Astrometric Lensing - What Gaia can and cannot do

Giorgi Kokaia

Lund Observatory
Lund University

2014-EXA80

Degree project of 60 higher education credits (for a degree of Master)
May 2014

Supervisors: David Hobbs
Lennart Lindegren

Lund Observatory
Box 43
SE-221 00 Lund
Sweden

Populärvetenskaplig Sammanfattning

Den 19e december 2013 skickades satelliten Gaia upp i rymden från Franska Guyana. Gaias uppdrag är att mäta position, avstånd och rörelse för ca en miljard stjärnor och detta kommer den att göra över de nästkommande 6 åren. Mycket av de primära vetenskapliga uppgifterna är redan avklarade och håller påatt testas, men Gaia är ett väldigt stort projekt vilket innebär att mycket vetenskap kan uppkomma vid sidan om det primära. Detta masterprojektet är just det. Det har varit känt i nästan 100 år att gravitationsfält böjer ljus som passerar förbi och målet med detta projektet var att utröna huruvida denna effekten går att använda för att studera Galaxen. Anledningen till att man vill göra detta är att Galaxen är fylld med mörka kroppar såsom bruna dvärgar (stjärnor som inte är massiva nog för fusion), svarta hål och neutronstjärnor (dessa tvåär slutprodukter i massiva stjärnors liv). Dessa kroppar är väldigt svåra, om inte omöjliga att detektera annars vilket är problematiskt dåobservationer av dessa kroppar är viktiga för att förståformationshistorian för de minst samt mest massiva stjärnorna i Galaxen. I detta projektet såhar ramverket AGISLab skapat för att simulera olika delar av Gaias uppdrag användts för att simulera observationer som påverkas av kroppars gravitationsfält. I koden sålades det till en metod för att simulera ljusavböjning enligt den såkallade ljusavböjningsekvationen. Samtidigt såimplementerades en metod för att återfålinsens parametrar (massa och position) medan Gaia utför en observation. De olika testen som utfördes bestod av 1) Hur långt ut Gaia kan detektera en lins 2) Om detekterad, hur väl kan man återfålinsens parametrar 3) Hur väl kan massan påsynliga kroppar bestämmas. När dessa saker testades såanvändes till stor del modifierade men redan existerande metoder AGISLab. I det frsta testet såvisade det sig att våra antaganden och krav hade varit för strikta, om man gör dem lite mindre strikta såkan man komma upp i $\sim$5 deteketioner. Resultaten för test tvåoch tre visar desvärre att ingen av dessa sakerna fungerar tillräckligt väl för att vara användbara i realistiska scenarion. Slutsatsen man får dra är därimot inte att Gaia inte klarar av detta utan att det måste utvecklas nya verktyg för att dessa effekter ska gåatt detektera.

Abstract

Context: Data from the recently launched astrometric satellite Gaia will be coming in soon with the final data release expected in 2022. This will provide a very precise map of the Galaxy. The Solar system and Galaxy is thought to be filled with invisible bodies (planetesimals, planets, brown dwarfs, neutron stars, black holes, etc.) and they will affect the observations via gravitational lensing.
Aim: I investigate to what extent it is possible to use gravitational lensing to study the otherwise invisible bodies. Also investigated is the possibility of determining masses for visible bodies for which it otherwise is hard to directly determine the mass of.
Method: I utilize the existing Gaia simulation and testing environment to simulate observations which are perturbed by placing a massive body in the line of sight. Three tests are conducted: In the first test the observation finishes without trying to adjust for the body, this leaves traces of the lensing in the observational residuals. This simulation is repeated whilst the body is moved further out in order to determine at what distance the traces of a body of a given mass no longer appears in the residuals. In the second test an attempt fit a 3D lensing model to a lens that is detected in the residuals is made. In the third test the position of the lens is assumed to be known and only the mass is attempted to be recovered.
Results: I find that the detection scaling for the mass-distance relation is highly dependent on the chosen line of sight and assumed stellar density. With the assumptions calculations show that there will be on the order of ~ 0.004 detections. Doing the fit with both position and mass was found to be very difficult due to the data reduction utilizing a linear algorithm whereas the problem is highly non-linear. The mass determination works better but becomes unstable at large distances leaving few interesting bodies of which mass can be determined.
Conclusions: The detection criterion was strict. Relaxing it and redoing the calculation gives ~ 4 detections. The predictions is however very sensitive to the assumed density of sources close to the lens and can thus vary by orders of magnitude. I also argue that one should differentiate between the detection of a lensing event and the detection of a lens in these discussions as many more lensing events will be detected than can be confirmed as lenses. For this reason alternative methods of detection are discussed.

Contents

Introduction

In this project I investigate the effect of gravitational lensing on the observations made by the Gaia satellite. The primary application under investigation is the possibility of detecting massive bodies that are too dim or otherwise impossible to be observed conventionally, by instead looking at their gravitational deflection of light. This is investigated by simulating the observations that Gaia will do whilst having a body in the line of sight deflecting light, perturbing the observation.

In the first chapter of this work I discuss how astrometry works. Beginning with some historical context then moving on to how astrometry works and then finally how Gaia will do preform the astrometric measurement. After that comes a description of how the observed data is reduced and solved for. Finally the simulation framework used is discussed.

The second chapter covers how gravitational lensing works and what kind of lensing is of interest in this work. Also covered is what types of lenses are of interest for this work, their prevalence in the Galaxy and what could be learned by studying them. Finally the chapter a secondary application of gravitational lensing is discussed, the determination of masses of bodies deflecting light.

In chapter three the light deflection equations used in this work are derived and compared with the existing, more general light deflection equations (they introduce a lot more complexity to achieve higher accuracy which was not needed for this work). After that their implementation is discussed.

Chapter four starts of by discussing the stability of and the use of certain options in the simulations and shows that they are only stable under very specific conditions. Following that are the simulations done under these specific conditions because even though the they only work under these specific conditions they still give useful results. The results of the simulations are presented and then using those results calculations are made to predict the detection rates for Gaia. The results are then discussed also discussed is how the results would change under different assumptions. In parallel to these simulations another set of simulations are run in which mass determinations are attempted. These simulations are shown to be unstable and in the end alternate methods of determining masses are discussed.

Chapter 1

Background

The Gaia satellite was successfully launched on December 19th, 2013, by ESA. Gaia is the successor to Hipparcos which was launched in 1989. These are both astrometric satellites, i.e. the main science mission of both satellites was the measure of position, motion and distance to stars. Hipparcos did this for 120 000 objects at an accuracy of $\sim$1 milliarcsecond (mas) (Perryman & ESA, 1997), which is the equivalent of having a 10% error in the distance measure of a star at 100 parsecs. This means that reliable distance measurements are only available in the Solar neighborhood. But we are about to enter a new era, the era of Gaia and this will lead to great advances in all fields of Galactic astronomy. This because Gaia will measure 10 000 times as many objects with more than 100 times greater accuracy up to $\sim$8 microarcseconds (μas). This means that Gaia will measure the positions and velocities of 1% of the stars in the Milky Way from which astronomers will be able to extrapolate a full 6D-map of the Galaxy (6D refers to a map containing x, y and z positions and the velocities in these directions). When this information is combined with other large surveys currently underway (such as the Gaia-ESO survey), it will give an even more detailed map; sometimes referred to as a "12D-map" i.e. a map which includes the 6 aforementioned parameters but also chemical abundances and stellar parameters such as temperature or surface gravity. This is great in itself, however, as with any other large scientific endeavor it is impossible to know what other kinds of science will be possible to do in the peripheries of the main science goals.

The aim of this project is exactly that, to look at one particular effect, see if it can be observed in the Gaia data and then see if it could give any science. The effect being looked at is the astrometric shift induced by gravitational lensing, as described in Section 2.2 and the goal is to determine whether it is possible to use this effect to detect otherwise invisible objects such as planets in the outermost part of the solar system, nearby stellar black holes and also galactic intermediate mass black holes. Further, if this astrometric shift is detected in the data the possibility of solving for this kind of body is explored, i.e. determining its mass and position. From the determination of the lens properties another possibility arises and that is using the exact same methods but for determining the masses of visible bodies for which it otherwise is very hard or impossible to directly determine the mass.

1.1 Astrometry, A historical perspective

The positions of stars have been measured and cataloged over many centuries with the first ones dating back to ancient Greece. It was not until the 19th century that Friedrich Bessel was able to determine the first stellar parallax (the defenition of stellar parallax is shown in Fig. 1.2). Before Bessel Edmond Halley had noted that stars were not stationary by comparing his measurements with those by Ptolemy 2000 years prior. This was a phenomenon which had been observed before but only for

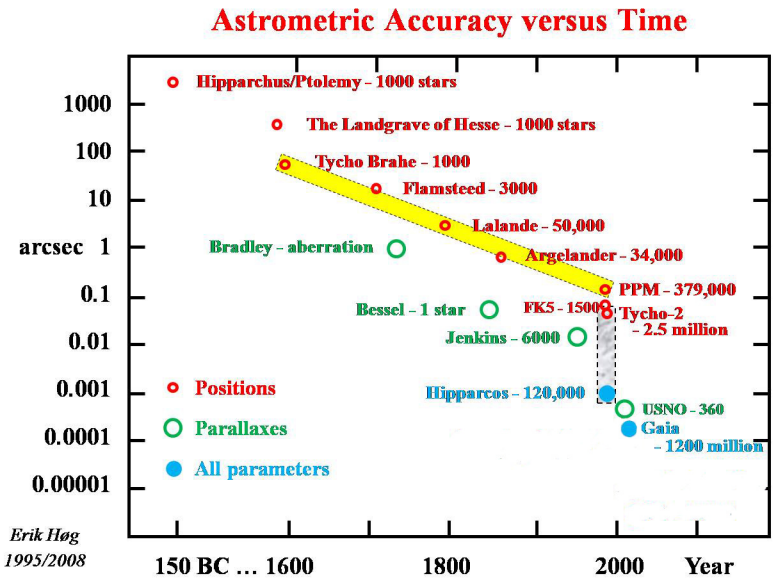

Figure 1.1: Cataloging positions and brightness of stars is one of oldest systematic studies in astronomy. The figure above shows how this has changed through history, with increasing accuracy and size of catalogs. It can be seen in the figure that Gaia a jump in accuracy but more notably a jump in the size of the catalog. It can be seen that Hipparcos also made a significant jump, the jump Hipparcos made was due to it being the first astrometric space mission combined with the advent of CCDs. The jump Gaia makes is in large part from the lessons learned during the Hipparcos mission. Image credit: E. Høg (1995)

the planets (from ancient Greek, *ἀστήρ πλανητής*; astēr planētēs - wandering star). It contradicted the long standing notion that the stars were stationary. What Bessel then did was to meticulously measure the motion of a single star (61 Cyg) and when he saw the trajectory of the star he realized that this was a combination of the star's own motion and the Earth's motion around the Sun which meant that it could be used as a distance measure.

The fact that this had not been measured before is not that strange, the accuracy that Bessel had to achieve in order to measure the parallax was 0.1 arcsecond. A degree is split up in 60 arcminutes and an arcminute is in turn split up in 60 arcseconds, which means that an accuracy of $\sim 3 \times 10^{-5}$ degrees had to be achieved in order to measure this effect. This is equivalent of measuring the size of a match from a distance of 50 km (in contrast to this, Gaia is able to measure the size of a match on the Moon from Earth). Figure 1.1 shows the development of astrometry through history.

1.2 Astrometry, A brief overview

The purpose of astrometry is to measure the position on and motion across the sky of a given object. When applied to a star it will also utilize the Earth's motion around the Sun to measure the parallax of the star. This means that as a star is observed it will exhibit elliptic motion as shown in Fig. 1.2. Not shown in the figure is the radial motion of the star. Gaia will measure radial velocity spectroscopically, so for the astrometry it can almost always be assumed to be known.

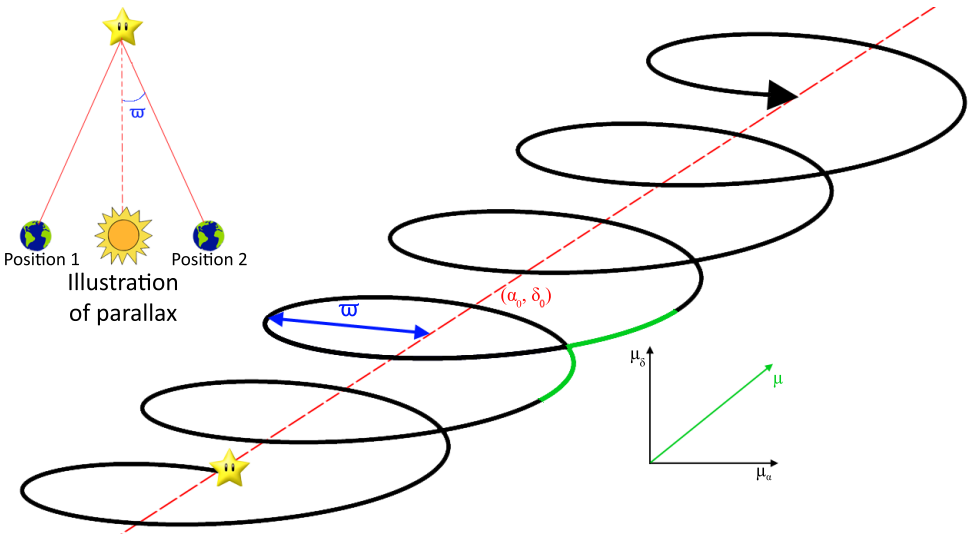

Figure 1.2: α_0 and δ_0 is the position of the source given at the reference epoch, which for Gaia is the mid-mission time. The elliptic motion of the source is due to the motion of Gaia around the Sun, the size of the ellipse that is drawn will depend on the distance to the source, which makes the half-angle ϖ (parallax) a distance measure. The source will also have a measurable motion relative to the Solar system which is separate from the parallax motion. This is called *proper motion* and the motion in the two directions are given as μ_α and μ_δ.

1.3 Astrometry with Gaia

After the successful launch the rocket placed Gaia in an orbit around the L_2 Lagrange point. L_2 is located 1.5 million km from Earth in the anti-direction of the Sun. There are a number of reasons for having Gaia at L_2, one of the primary of which being the fact that a test particle orbiting the Sun at L_2 will complete an orbit at the same time as Earth. This means that the Earth and the Sun will always be aligned from Gaia's point of view which in turn means that Gaia's Sun shield always can be oriented in such a manner as to block out the light.

Gaia will stay in a Lissajous orbit around L_2 for at least 5 years and whilst doing this it will also slowly rotate around its spin axis and also precess around the Sun. The precession and the rotation are shown in Fig. 1.3.

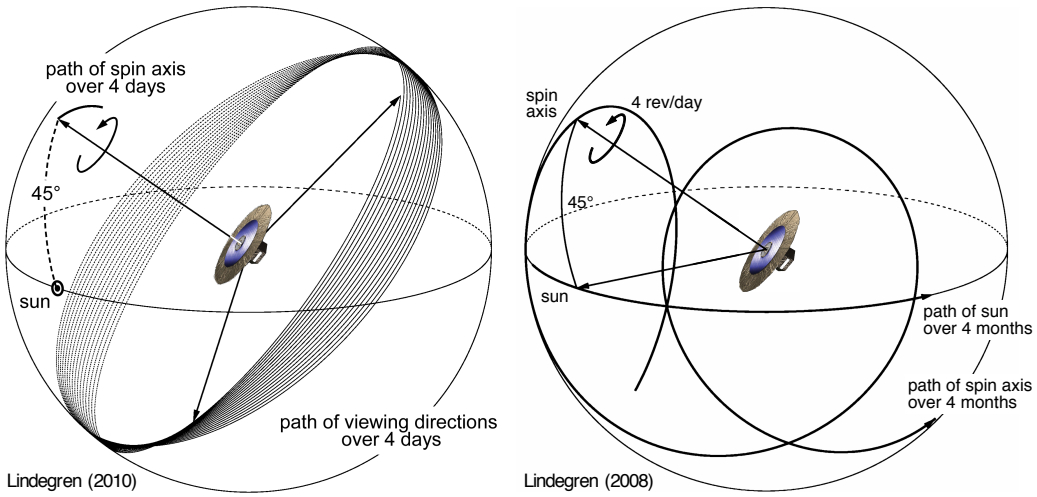

Figure 1.3: The figures depict two components of how Gaia scans the sky. The right panel shows how Gaia will be scanning the sky due to its own rotation and the motion around the sun. The rotation axis of Gaia is angled with respect to the Sun it will precess with a period of around two months. The left panel shows the scanning with the precession included, because of the precession the scanning will not be done in closed circles but instead it will do spirals meaning it will cover a larger part of the sky. The combination of these two things is known as the Nominal Scanning Law. Credit: ESA

The combination of the rotation, precession and orbit results in a complex coverage of the sky, which is shown in the middle panel of Fig. 1.4. In the top panel a simulated stellar density of the Galaxy is given and in the bottom panel the combination of the two is given. This figure is quite important because as it will become apparent later on, the observed source density assumed and the direction one looks in in the various tests are important parameters.

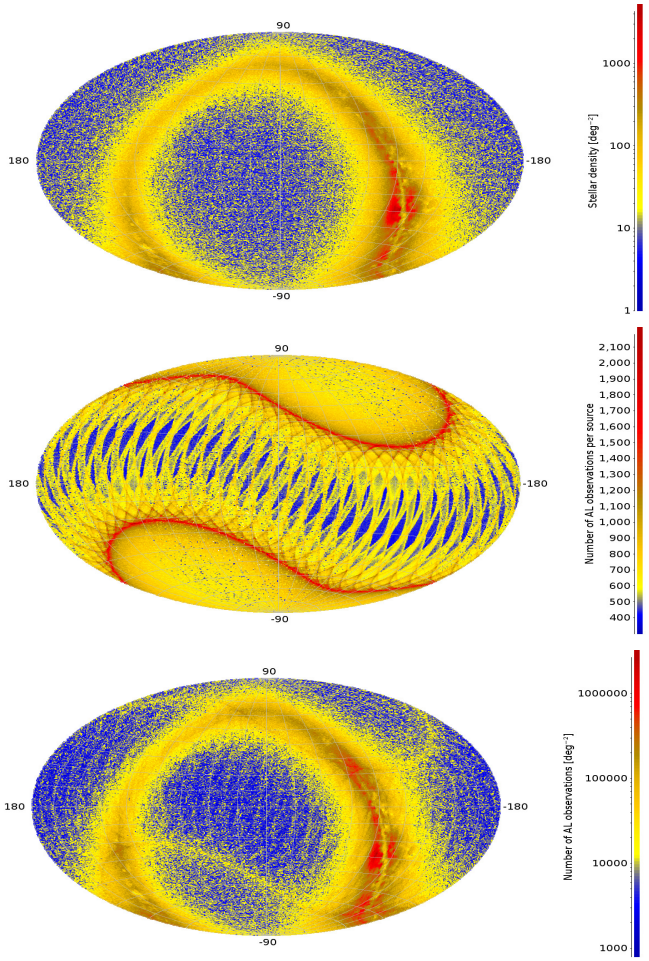

Figure 1.4: All-sky projections of (from top to bottom) the source density using 2 million sources (actual density will thus be a factor ∼500 greater), the number of observations per source and complex sky coverage, and the resulting spatial density of observations. Image credit: Lindegren et al. (2012)

1.3.1 Astrometric Global Iterative Solution (AGIS)

In the following section a description of the the global solution, AGIS (**A**strometric **G**lobal **I**terative **S**olution) will be given; for a more in depth review see Lindegren et al. (2012). One of the key lessons learned from Hipparcos was that when attempting to construct a global reference frame, having simultaneous measurements of sources separated by a large angular distance greatly increases the accuracy of the reference frame. For this reason Gaia observes in two fields of view separated by a large angle which we refer to as the basic angle. The observations are then put in the reference frame which is constructed by selecting a subset of $\sim 10^8$ 'well-behaved' sources. In this case well-behaved simply means that the proper direction of the source is accurately modeled by the astrometric model outlined in Fig. 1.2; i.e. we assume uniform space motion of a single source, neglecting binary systems and Galactic acceleration. Once the subset, also known as the primary sources, has been selected it can be used for the astrometric core solution. The core solution is in essence a multivariate least square optimization for all the parameters used to model the observations. The parameters are divided in four groups:

- The astrometric parameters, representing the position of the observed sources as a function of time.

- The attitude parameters, representing the orientation of the satellite in the reference frame as a function of time.

- The calibration parameters, which are used to correct errors of the instrument with respect to the ideal geometry.

- The global parameters, representing things that affect all observations, such as hypothetical deviations from general relativity.

These parameters are all in some way dependent on each other. Combining this with the fact that data from $\sim 10^{11}$ observations (amounting to ~ 70 TB of data) will be used for the solution makes finding a direct solution impossible. Thus the problem was formulated in such a manner that an iterative solution could be found. Generally, any least-squares optimization problem can be written as:

$$\min_{s} ||\mathbf{f}^{\text{obs}} - \mathbf{f}^{\text{calc}}(\mathbf{s})||_{\mathcal{M}} \tag{1.1}$$

Here $\mathbf{s}$ is a vector of the unknown parameters that are of interest. In this case $\mathbf{s}$ includes both the astrometric parameters and the other, so called "nuisance parameters", described previously. $\mathbf{f}^{\text{obs}}$ represents the observed data as mapped by the detectors at a specific time and $\mathbf{f}^{\text{calc}}(\mathbf{s})$ is the modeled observation, e.g. how we expect the detectors to map the observation as a function of astrometric and nuisance parameters. $\mathcal{M}$ represents the metric defined by the statistics of the data in which the norm is calculated.

The main concern for solving Eq. 1.1 is the modeling of $\mathbf{f}^{\text{calc}}(\mathbf{s})$. Figure 1.5 shows the steps taken in modeling $\mathbf{f}$. Appendix B briefly shows how the normals are determined which then are used in the solution.

Reference system

Before discussing how the astrometric model is constructed we must specify in which reference system we want to construct it. The high astrometric accuracy aimed for with Gaia necessitates the use of general relativity when modeling the data. This means that we need to be precise in our descriptions of the motion of Gaia, the source and the path traveled by the light and we also need to be specific in the transformation between the different reference frames. The relativistic framework Gaia utilizes (Klioner, 2003, 2004) is described further in Appendix A, but there are some concepts which the reader should be aware of.

The light propagation and the motion of Gaia are modeled in the Barycentric Celestial Reference System (BCRS). This is a reference system with its spatial origin in the barycenter of the solar system whilst aligned with the International Celestial Reference System (ICRS, Feissel & Mignard, 1998) and the temporal axis centred on the mid-mission time (2017.0, given in barycentric time, TCB). However, in order to properly model the attitude and the celestial direction in which the source is observed it is also necessary to introduce a reference frame which is co-moving with, centered on and uses the proper time (T_G) of Gaia. Klioner (2004) shows how such a reference system, which is also aligned with ICRS and kinematically non-rotating can be constructed; we refer to this as the Centre-of-Mass Reference System (CoMRS).

Astrometric model

The astrometric model is what we use in order to model the coordinate direction $\hat{\mathbf{u}}_\mathbf{i}(t)$ of source i at time t (TCB) using the astrometric parameters $\mathbf{s}_i$. When modeling the position of the star we assume it to be moving with uniform space velocity relative to the solar system, this means that we can model their position (in the BCRS) as:

$$\mathbf{b}_i(t) = \mathbf{b}_\mathbf{i}(t_{\rm ep}) + (t - t_{\rm ep})\mathbf{v}_i \tag{1.2}$$

where $t_{\rm ep}$ is the reference epoch and $\mathbf{b}(t_{\rm ep})$, $\mathbf{v}_i$ define the kinematic parameters of the source. However, for convenience sake we use the transformation of these parameters (as shown in Fig. 1.2) to describe the position of a star. They are contained within $\mathbf{s}_i$ and are:

- α_i the barycentric right ascension at the reference epoch
- δ_i the barycentric declination at the reference epoch
- ϖ_i the annual parallax (see Fig. 1.2)
- $\mu_{\alpha_* i} = \frac{\partial \alpha_i}{\partial t}\cos\delta_i$ the proper motion[1] in right ascension at the reference epoch
- $\mu_{\delta i} = \frac{\partial \delta_i}{\partial t}$ the proper motion in the declination at the reference epoch
- Finally, we have $\mu_{ri} = v_{ri}\varpi/A_u$ which is the radial proper motion at the reference epoch expressed in the same unit as the transverse components of proper motion (A_u is an Astronomical Unit). However as stated before, this quantity will in general be ignored as it is hard to measure accurately using astrometry. Instead, this quantity will be considered to be known from spectroscopy if the star is bright enough, otherwise it will be set to zero when setting up the astrometric model.

To get $\hat{\mathbf{u}}_i(t)$ out of these parameters, the same equation is solved as that for Hipparcos (Lindegren et al., 1992):

$$\hat{\mathbf{u}}_i(t) = \langle \mathbf{r}_i + (t_{\rm B} - t_{\rm ep})(\mathbf{p}_i\mu_{\alpha* i} + \mathbf{q}_i\mu_{\delta i} + \mathbf{r}_i\mu_{ri} - \varpi\mathbf{b}_{\rm G}(t)/{\rm A_u}\rangle \tag{1.3}$$

Here $\mathbf{b}_{\rm G}(t)$ is the barycentric position of Gaia at the time of observation and $t_{\rm B}$ is the barycentric time, given by correcting for the Römer delay, calculated using: $t_{\rm B} = t + \mathbf{r}_i \cdot \mathbf{b}_{\rm G}(t)/c$ where c is the speed of light. The angular brackets represent vector normalisation, and $[\mathbf{p}_i,\ \mathbf{q}_i,\ \mathbf{r}_i]$ is the normal triad of the source with respect to the ICRS (Murray, 1983). $\mathbf{r}_i$ is the barycentric coordinate direction at the reference epoch, $\mathbf{p}_i = \langle \mathbf{Z} \times \mathbf{r}_i \rangle$ and $\mathbf{q}_i = \mathbf{r}_i \times \mathbf{p}_i$. Their components in the ICRS are given by the matrix:

$$[\mathbf{p}_i,\ \mathbf{q}_i,\ \mathbf{r}_i] = \begin{bmatrix} -\sin\alpha_i & -\sin\alpha_i\cos\alpha_i & \cos\delta_i\cos\alpha_i \\ \cos\alpha_i & -\sin\alpha_i\sin\delta_i & \cos\delta_i\sin\alpha_i \\ 0 & \cos\delta_i & \sin\delta_i \end{bmatrix} \tag{1.4}$$

This model is derived in a purely classical framework using Euclidean coordinates and besides the Römer delay, light propagation is not considered. It has been shown that this is sufficient to model the observations at a sub-microarcsecond accuracy. The transformation of the observation to the CoMRS and the modeling of light deflection as light enters the Solar system requires the use of general relativity, this is described in Appendix A.

[1] Angular velocity over the sky, usually given as $mas\ yr^{-1}$. The $\cos\delta_i$ comes from the fact that α is the longitudinal coordinate and the size of each step in α will vary with the latitude, δ

Attitude model

The attitude model is what we use to model the instantaneous position, orientation and direction of the spacecraft. The craft is designed to follow a specific attitude, in this case it is the Nominal Scanning Law, as shown in Fig. 1.3. This is defined analytically for an arbitrarily long time, but there will be deviations from this attitude by up to one arcminute in all three axes and depending on the type of perturbation on the craft the duration of deviation will vary from seconds to minutes. Te CCD integration time is 4.42 s this means that the physical attitude will not be measurable, only a smoothed version of it which depends on the CCDs. This means that for the desired accuracy to be achieved the attitude must be possible to model whilst computing the astrometric model; this is achieved by modelling the attitude using a finite number of attitude parameters. For the mathematical description of this modeling see Lindegren et al. (2012) since it will not be detailed here, as for this project the attitude was always assumed to be known. How and why this works is discussed later.

Calibration model

The calibration model is used to express the precise locations of the CCDs as a function of the field angles (η, ζ). Several different factors contribute to how this will look, including: the physical geometry of each CCD, their positions in the focal-plane assembly, distortions due to slight variations in the basic angle Γ_c, etc. Most of the variations that will arise during the mission are expected to be smooth functions of the field angles, however some effects (such as geometry of the pixel columns) will be irregular and evolve on varying time scales. So the calibration model has been constructed in such a manner that it can take both of these into account.

Global model

In the solution we can incorporate an arbitrary number of global parameters. These are parameters that affect all of the observations but are not directly related to the spacecraft nor the astrometric model. An example of such a parameters is PPN-γ (Eq. 3.8), which is a parameter that measures how much light is deflected by rest mass. The effect they represent is then included when simulating the observations and the task of the global block is to match this effect using the partial derivatives of the equations in which the parameters appear in order to recover them. During the real mission the same equations can be used to test general relativity.

Velocity model

When doing the transformations and calculations in the data reduction it is important the barycentric position and velocity of Gaia is known to a high precision. These things will be monitored with radio interferometry and optical telescopes. However, the observations might not be sufficient in all cases and for those cases this block has been developed. It takes the observations and data and models the velocity and position of Gaia.

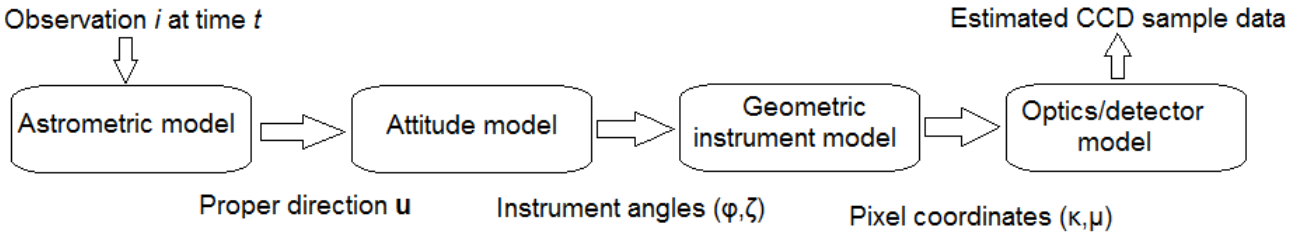

Figure 1.5: A simple schematic representation of the main steps needed in order to model the observed data.

1.3.2 AGISLab

AGISLab is a platform that has been developed for and is being used for development and testing of AGIS. It is a scaled down version of AGIS, which means that the number of sources required to do the data reduction can be much smaller than the $10^7 - 10^8$ primary sources used in the actual solution. This makes the testing of new ideas and algorithms much more manageable as they are developed.

The way AGISLab works is summarized briefly in the bullet points below; following them is a more detailed description.

1. A set of true sources is generated, which can be seen as a noiseless stellar background; depending on what is being tested different stellar backgrounds can be generated.
2. Noise is added to each source, giving us the so called (initial) running sources.
3. The same thing is done in the other blocks: a true value is generated to which noise is added
4. The observation of the sources and the behavior of Gaia is simulated.
5. All of the parameters are then given to the corresponding processor which sets up the least-squares problem discussed in the previous section.
6. The least-squares problems of each block are combined and given to the main algorithm which iterates the solutions to convergence. If the problem is sufficiently linear (which the main data reduction problem is) a conjugate gradient algorithm is turned on, which greatly increases the speed at which you reach the solution. Otherwise, simple iterations are used.
7. If the solution converges then we can find the error in each parameter. The error is the difference between the running source and the true source. Of course the error will not be known in the real mission, but for testing purposes it is quite useful.

Figure 1.6 outlines how these steps work in greater detail. The first thing we see in each block are the true values for the parameters in the blocks. The true values are the input values and the purpose of AGISLab is to give us the tools required to investigate how we can best recover the true values.

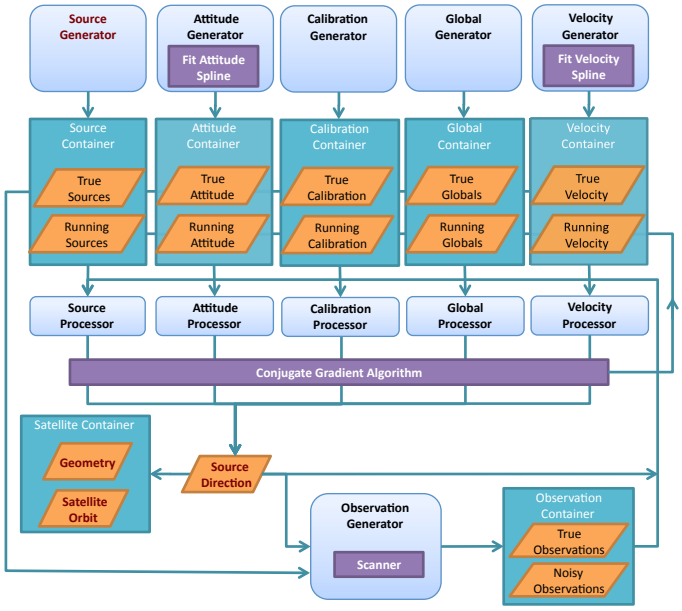

Figure 1.6: A schematic representation of the different parts of AGISLab.
Credit: Holl (2009)

The reason we use AGISLab and not AGIS for testing was touched upon in the beginning of this section. The whole process described previously could just as easily be done using AGIS as long as a generator for observations was added to it. As stated previously, AGIS was designed to reduce the real Gaia data which means that it has to use some $\sim 10^8$ primary sources. This makes AGIS bad for testing purposes, since we are interested in running the simulations many times over whilst varying different conditions and parameters. If we were using AGIS this would be very time consuming and that is where AGISLab comes in.

AGISLab is designed in such a manner that it only needs $\sim 10^6$ sources to fully reconstruct the attitude of the satellite. Even though we can work with a factor of 100 less sources, running the simulations multiple times is still time consuming. That is why there exists a scale factor, S, which is used to set what fraction of primary sources to be used in a run. For example if $S = 1$ then 10^6 primary sources are used and if $S = 0.1$ then 10^5 primary sources would be used. However, we cannot expect to simply scale down the number of primary sources and in doing so recover the same results which means that the scale factor has to do more than simply scale the number of primary sources (see Holl, 2012, for full discussion).

In order to scale down the simulation whilst maintaining the validity of the observation other properties that are affected by the scaling must be looked at. These include the number of transits for a given primary source, number of primary sources in a field of view at a given time and the mean number of transits. All of them can be resolved by changing a single factor, as we scale down the number of sources we also scale up the field of view. To illustrate this we can look at Fig. 1.7, which shows a single source crossing the focal plane. In reality there would of course never be a single source on each CCD but a large number of them. The number of sources per CCD at a given time is one of the the things that we aim to keep constant as we scale the simulation up and down. This could of course be done by scaling the size of the CCDs as we scale the simulation but that would bring with it other complications such as affecting the speed at which a source moves across a given CCD. If instead we change the focal length of the observation, the speed at which sources move across the CCD, how

often it crosses and how many crossings are done in a given time span remain unaffected.

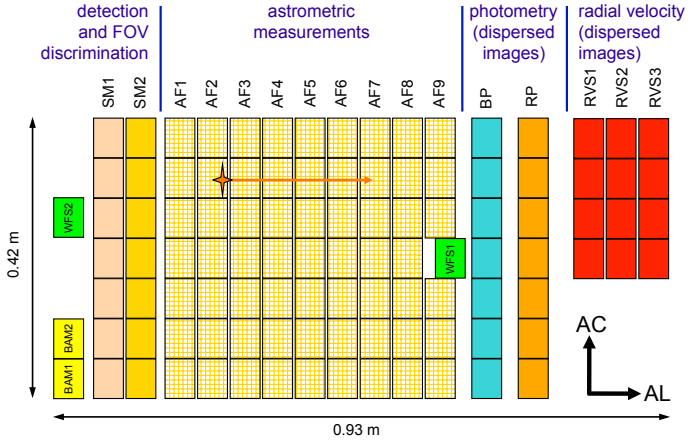

Figure 1.7: A schematic representation of the CCDs in the focal plane of Gaia. Depending on the attitude of Gaia a source will enter on the left at some across scan (AC) position. They will first be picked up by the skymappers (SM1 and SM2) which are responsible for the selection process, i.e. whether the source will be tracked as it moves in the along scan (AL) direction. If selected the source is then tracked along the CCDs dedicated to astrometry (AF1-9) photometry (BP and RP) and radial velocity-determination (RVS1-3).
Credit: Holl (2012)

Chapter 2

Gravitational Lensing

2.1 History

Gravitational lensing is a phenomenon predicted by general relativity; it states that a gravitational field will bend the path of a photon propagating through it. This was one of the bolder statements made by general relativity since it had been known for a long time that light always travels the quickest path between two points in space (first proposed by Alhazen 1021 AD, later generalized by Fermat). However, gravitational lensing does not contradict Fermat's principle since the light does travel in a straight line, but in the presence of a gravitational field, the space in which the light travels is bent, changing the path of the photon. This was the second prediction by general relativity that was validated experimentally (first one being the precession of Mercury), it was done by Arthur Eddington in 1919 (Eddington, 1919) in an experiment where he observed the position of stars at night and then observed the same stars as the Sun was passing close by them during a Solar eclipse. He found that the position of the stars had changed as predicted by general relativity.[1]

Up until 1979 gravitational lensing had been viewed as a peculiar but not so useful result of general relativity. Zwicky (1937) did however suggest that distant galaxies could be viewed using this method, but his suggestion went unheard by most. The discovery of the doubly imaged quasar Q0957+561 in 1979 not only sparked an interest for gravitational lensing amongst astronomers but it also spawned an entirely new branch of observational astronomy.

2.2 Overview

Normally, gravitational lensing is modeled using the so called thin lens approximation. In this approximation one uses the fact that the extent of the lens along the line of sight is so much smaller than the distance between the observer and the background source that the lens can be considered a point along the line of sight. One also assumes that all the lensing occurs when the light passes by the lens. This is not fully representative of what actually happens, but it is still useful to look at when considering lensing because of its simplicity and accuracy. Figure 2.1 depicts this approximation, in it some angles and distances have been marked, which are used for the mathematical formulation. Here follows a derivation of the deflection equation. From the figure it can be seen that in a circularly symmetric case it would be, given by the gravitational influence from a point mass on the trajectory

[1] To be exact, his findings were not in full agreement with general relativity but the predictions of general relativity were within his margins of error.

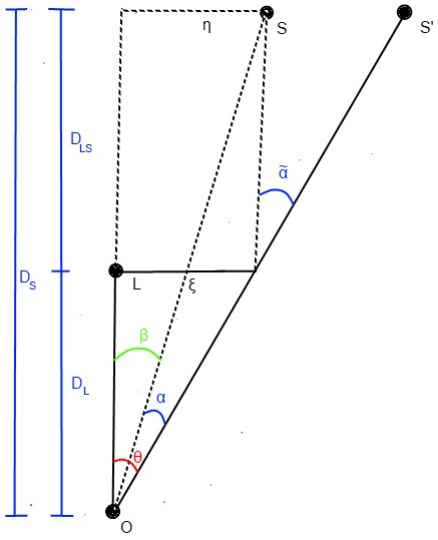

Figure 2.1: An illustration that depicts the thin lens approximation. Besides the varius lengths and angles marked, O shows the position of the observer and L the position of the lens. S and S' are the true and apparent positions of the source being lensed.

of a light ray:

$$\hat{\alpha}(\xi) = \frac{4GM(\xi)}{c^2}\frac{1}{\xi^2} \tag{2.1}$$

where $M(\xi)$ is the mass enclosed within the so called impact parameter, ξ. In the figure, one can easily see that the relation shown below must hold for small angles (which is the case for almost all astrophysical applications):

$$\theta D_S = \beta D_S + \hat{\alpha} D_{LS} \tag{2.2}$$

Then, expressing the deflection angle as:

$$\alpha = (D_{LS}/D_S)\hat{\alpha} \tag{2.3}$$

From Fig. 2.1 we see

$$\beta = \theta - \alpha \tag{2.4}$$

Rewriting Eq. 2.4 using the Eq. 2.3 equation gives the so called lens equation:

$$\beta = \theta - \frac{D_{LS}}{D_L D_S}\frac{4GM}{c^2\theta} \tag{2.5}$$

We can now define the so called Einstein radius,

$$\theta_E = \sqrt{\frac{D_{LS}}{D_L D_S}\frac{4GM}{c^2}} \tag{2.6}$$

which is the characteristic lensing angle and most lensing events will be in the same order. Using this, Eq. 2.5 can be simplified to:

$$\beta + \frac{\theta_E^2}{\theta} = \theta \tag{2.7}$$

which then is further simplified by normalizing all the angles with θ_E, so that $\beta \equiv r_s\theta_E$ and $\theta \equiv r\theta_E$, which gives:

$$r_s + \frac{1}{r} = r \tag{2.8}$$

Since the equation has two solutions, this means that for every case except perfect alignment ($r_s = 0$) two images will appear. In most cases however only one image can be seen, this is described further down on this page. The two images will be located at:

$$r_\pm = \frac{r_s \pm \sqrt{r_s^2 + 4}}{2} \tag{2.9}$$

In the case of $r_s = 0$ we get a so called Einstein ring, as shown in Fig. 2.3. Equation 2.9 shows that one of the images, which will be called the '+' image, will appear outside the Einstein radius, shifted outward in the lens-source direction ($r_s > 1$) and the '-' image will appear on the inside of the Einstein ring on the opposite side of the lens.

2.3 Different types of lensing

Gravitational lensing is categorized in three different types of lensing, dependent on the line of sight density, i.e. the enclosed mass within an area on the sky of the lens and the types of lensing are briefly discussed here:

- Strong lensing
  Strong lensing occurs when the surface density of the lens is above the so called critical density in combination with the lensed source being sufficiently bright, when this is the case, one of two things can occur. If the lens and source are perfectly aligned the source will be completely distorted and a so called Einstein ring will appear, if they are not perfectly aligned the source will be multiply imaged. These cases are shown in the figures below.

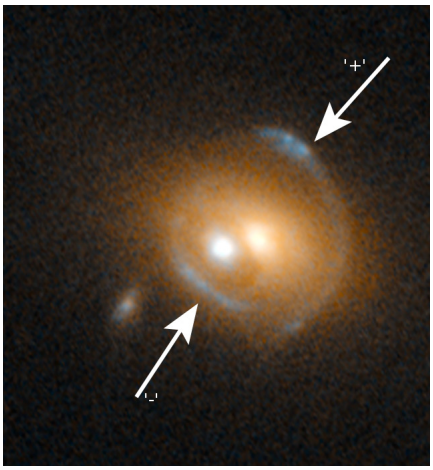

Figure 2.2: Depicted above a twicely imaged quasar(SDSS J0919+2720) and it a behavior very similar to that described in the previous section. The difference is that the shape of the sources look distorted, this is because the gravitational field of the lens (foreground galaxy) is not perfectly spherically symmetric.
Credit: ESA/NASA & Hubble

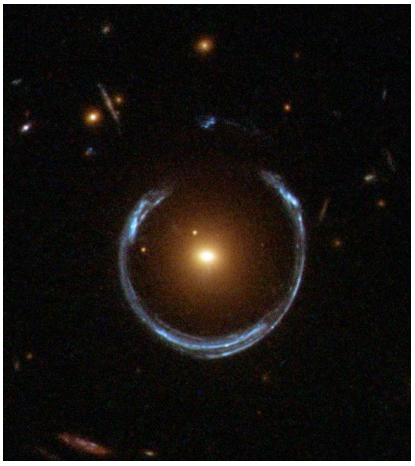

Figure 2.3: Depicted above is the special case in which the lens and the source (Horseshoe galaxy - LRG 3-757) are perfectly aligned. And as described in the previous section, an Einstein ring appears.
Credit: ESA/NASA & Hubble

- Microlensing
  Microlensing can refer to one of two things. Astrometric microlensing which is the focus of this work or photometric microlensing which refers to the magnification of sources which is discussed briefly in the next section. Microlensing occurs when the lensing effect is not sufficiently strong to produce two distinct images which could be because the secondary image is too faint or that they cannot be resolved as two separate images. This means that what one instrument may perceive as microlensing another may perceive as strong lensing. The same thing can be said about photometric and astrometric microlensing, what is seen depends on what the instrument is sensitive to. They are governed by different equations, but if one happens so does the other. Unlike strong lensing however, microlensing requires variability to be detected. Detecting a multiply imaged and/or deformed galaxy in your data immediately tells you that it has been strongly lensed. If it is microlensing that is happening, all that happens is that something is being shifted and magnified which means that if the lens has no relative motion to the source then it is impossible to know that the magnified/shifted source is not the true source. Luckily, the lenses we are interested in for this work have larger parallaxes than most stars so there will always be relative motion.

- Weak lensing
  There are cases when the effect of a lens cannot be seen when it lenses a single source. It was mentioned in the part about microlensing that if the lens is static it would be impossible to say whether it is a lensed source being observed. However, if there are a lot of sources being lensed very specific patterns will appear in them which can identify the presence of a lens. When that is the case it is called weak lensing.

2.3.1 Magnification

The reason for magnification occurring during gravitational lensing is that surface brightness is a conserved quantity.[2] It can be shown that the magnification is given by the ratio of the image area and the source area. Here follows a simple derivation of it.

For a point-like source the source annulus can be considered with a small angle ($\Delta\varphi$) and for a point-like lens this annulus will mapped into two annuli, one inside the Einstein ring and one outside. The area of the source annulus is given by the product of the radial width and the tangential length $dr_s \times r_s\Delta\varphi$ and the area of each image is then given by $dr \times r\Delta\varphi$ (with r_s and r defined as in the previous derivation). Thus, the magnification, μ, is given by:

$$\mu = \frac{dr_s \times r_s\Delta\varphi}{dr \times r\Delta\varphi} = \frac{rdr}{r_s dr_s} \tag{2.10}$$

inserting the values from Eq. 2.9 we find:

$$\mu_+ = \frac{(r_s + \sqrt{r_s^2+4})^2}{4r_s\sqrt{r_s^2+4}}, \quad \mu_- = \frac{(r_s - \sqrt{r_s^2+4})^2}{4r_s\sqrt{r_s^2+4}} \tag{2.11}$$

The total magnification can then be written as:

$$\mu = |\mu_+ + \mu_-| = \frac{r_s^2+2}{r_s\sqrt{r_s^2+4}} \tag{2.12}$$

2.3.2 Lensing in this project

Since Gaia is so much more sensitive to changes in astrometry than it is to photometry the focus of this work is on the astrometric part of the lensing. It is not referred to as microlensing because the lensing studied here will not always be producing microlensing events, in some cases we end up working in the weak lensing regime. Thus it is referred to in a more general sense as astrometric lensing. For the purpose of this work we have chosen to ignore the magnification and the reason for this is twofold. Firstly, as just mentioned, Gaia is a lot more sensitive to changes in astrometry, this can be illustrated by some simple calculations. The sky is 5.3×10^{11} as^2 and out of the 10^9 sources that will be observed Gaia, 10^8 sources will have sufficiently high accuracy in their astrometric parameters to be used in this project. This means that the average distance between sources will be 41.2 as. This distance can be used to estimate the average distance between lens and the nearest sources. Using this distance as the distance between the source and the lens and having the lens be a 1 $M_\odot$ body at 1 pc ($\theta_E \approx 90$ mas); we find that the average magnification will be ~ 1.00000000005, which is far too small to be measured. Whereas if the astrometric shift is calculated in a similar manner we get an average deflection of ~ 200 μas, within the sensitivity of the bright sources observed by Gaia.

Secondly, the luminosity of a source is something that is directly measured, whereas the position is measured and then calculated and put into a model. It is far easier to include and fit a model for a lens which causes an astrometric shift into the existing scheme than it would be to create a whole new infrastructure for such measurements.

There will of course be photometric lensing events, their potential use is discussed in Section 4.3.4.

[2] If an object appears to be deformed due to it being gravitationally lensed the total surface brightness will be the same as if it was not being deformed

2.4 Detecting invisible objects

The following section describes the types of objects that are investigated in this project, and the motivation for looking for them. What characterizes these objects is that they are too faint to be directly detected by Gaia or any other current survey. Then one must ask, what types of objects could this include? This project will explore objects in three mass ranges:

- Planetary to brown dwarf masses (up to 80 Jupiter masses, M_j) in the Solar system and neighborhood. The types of bodies in this category includes hitherto undetected planets in the outer Solar system and the possibility of a brown dwarf companion to the Sun. There are also objects not bound to the Sun in this mass range that should be considered, such as: nearby brown dwarfs that otherwise would be too faint to be discovered [3].
- A few to a few tens of Solar masses ($M_\odot$), the types of bodies in this category are primordial (e.g invisible) neutron stars and stellar mass black holes
- A hundred to a few tens of thousands Solar masses. The only type of body that falls in this category is intermediate mass black holes.

In the following sections it will be motivated why these objects might exist and the parameter-space to explore will be discussed.

2.4.1 Planetary mass companion

A strong case for the existence of a nearby invisible body can be made for the existence of one in or near the so called Oort Cloud. The Oort cloud is a spherical cloud of comets surrounding the Solar system. Its existence was first suggested by Jan Oort in 1950. Oort studied the trajectories long-period comets in the Solar system and found that these comets all have an aphelion of $2000 - 100000$ AU, whilst many of them had a perihelion of a couple of AU.

In the same paper Oort argued that there must be some mechanism to perturb the cloud to cause the observed stream of comets coming into the inner Solar system from the cloud for the first time. The mechanism suggested by Oort was perturbations by passing stars. Since then different mechanisms have been explored as an explanation, such as galactic tidal effects (Byl, 1983) or an unseen bound Solar system object ("Nemesis", Davis et al., 1984).

The geological argument

Davis et al. (1984) made a case for the existence of an unssen bound Solar system object by looking at the geological record for mass extinctions which had been analyzed the same year by Raup & Sepkopski (1984). In their study they found a strong periodicity (Fig. 2.4) of ~ 26 Myrs which was then used to support the hypothesis of a bound Solar companion.

To this day this has remained a controversial subject and papers are continually published that support and rebuke the various hypotheses. Recently a major revision was done to the geological time scale which means that the main argument for a bound Solar companion might have been invalidated in the process. Melott & Bambach (2013) re-examined their re-examination (Melott & Bambach, 2010) of the findings in Raup & Sepkopski (1984). The re-examination they did in 2010 expanded the time

[3] Brown dwarfs do not have any internal energy generation and they radiate as black bodies the flux will thus depend on their radius squared whereas the mass and therefore amount of energy depends on radius cubed. So more massive brown dwarfs cool more slowly.

span of the analysis to 500 Myrs which resulted in two thing; firstly the periodicity was modified by $\sim 3\%$ to ~ 27 Myrs which was expected due to changes since 1984 and secondly they found an even stronger periodicity. In their 2013 analysis they find that the change in geological time scales increases the spectral power of the periodicity slightly. However they argue that this points against the Nemesis hypothesis because the periodicity is *too strong*, since such a bound companion would have been perturbed by the Galaxy over 500 Myrs.

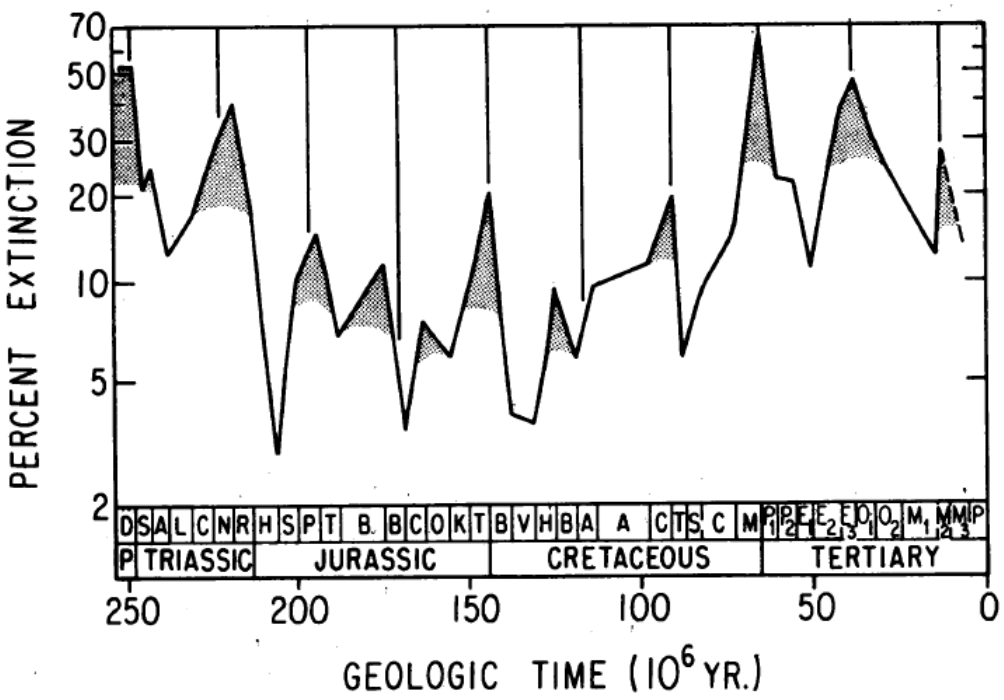

Figure 2.4: The figure above is the famous plot from Raup & Sepkopski (1984) which shows extinction fraction as a function of geological time. Time series analysis gives a periodicity of ~ 26 Myrs with $P < 0.01$.

The cometary argument

There are also astronomical cases to be made for the existence of large bound bodies beyond the Kuiper belt. In an analysis of the distributions of aphelia and other orbital elements of outer Oort Cloud comets anomalies were found (Matese et al., 1999). In a more recent study (Matese & Whitmire, 2011) they redid the analysis in the previous study but with a sample size almost double that of the original one. The anomaly persisted even in their larger sample, what they found was that $\sim 20\%$ of new comets (first time entrants in the solar system) have an originating aphelion along a great circle roughly centered at the on the galactic longitudinal bins 135°and 315°, these can be seen in Fig. 2.5 whilst Fig. 2.6 shows the great circle drawn on the skymap. Statistical analysis showed that it was unlikely for such an anomaly to arise simply from galactic perturbations. This lead to the conclusion that these anomalies would be best explained by a bound solar companion in the inner outer Oort Cloud, which they dubbed Tyche (Tyche is the good sister of Nemesis, the name was given to avoid confusion with Nemesis).

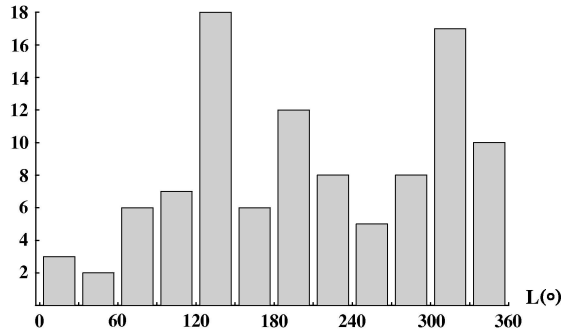

Figure 2.5: The histogram shows the origin in galactic latitude of comets
Credit: Matese et al. (1999)

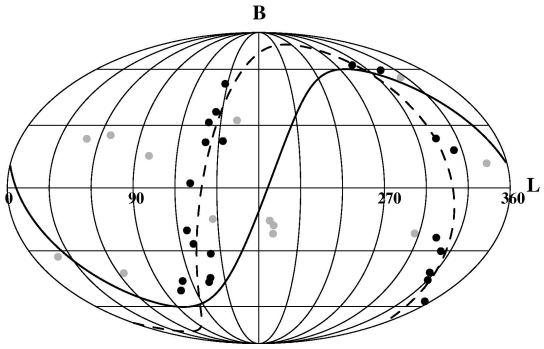

Figure 2.6: The origins of comets plotted on the skymap with a great circle drawn on top of them. The black dots show origins within $\pm 9.6°$of the circle, whilst grey ones show outliers that still have statistical significance
Credit: Matese & Whitmire (2011)

It should be noted that a Jovian mass gas planet will capture a significant amount of heat during its formation, which will not have been fully radiated away in the lifetime of the solar system (~ 4.5 Gyrs). Taking this into account, in the final data release of WISE (Wide-field Infrared Explorer, **?**)the authors of that study conclude that no planet more massive than Saturn could exist within 10 000 AU. This means that Tyche as suggested in Matese & Whitmire (2011) most likely does not exist. The apparent overabundance of comets along the great circle in Fig. 2.6 can still be seen as an indication of there being something out there, just not what the authors imagined.

Dwarf planet orbits

In a recent study (Trujillo & Sheppard, 2014) the discovery of a new Sedna-like object was presented. The authors noted that this new body has a similar perihelion argument ω[4] to other dwarf planets. Not only that, they found that most objects with a semi-major axis greater than 150 AU shared this similarity. Simulating the inner Oort Cloud they found that the distribution of ω should be random, which it clearly is not. One proposed possible solution to this is having a low albedo, ~ 10 $M_\oplus$ Super-Earth located at ~ 250 AU or something more massive farther away.

2.4.2 Relic neutron stars and black holes

These bodies are the end product of massive star evolution. Relic refers to the fact that these objects have been created continually through the lifetime of the Galaxy, and stayed there. They both share two qualities which make them good candidates for lensing studies: they have high masses and are in most cases virtually undetectable. Besides that their relic population in the Galaxy is quite numerous. Currently there are about 2000 known neutron stars in the Galaxy and most of them are young compared to it ($\lesssim 100$ Myr). The relic population is $\sim 10^9$ (Sartore et al., 2011). The large difference between these numbers come from the fact that they are hard to detect and that they only can be detected for a relatively short time. They can either be seen in an X-ray binary which has a relatively short lifetime and most of these bodies will never end up in an X-ray binary as their formation has a very high probability of disrupting the binary. Or they can be seen if their narrow radio beam happens to be pointed towards us. This also does not last long because they will spin down and as

[4]The orbital element ω describes the angle between the point of perihelion and where a bodys orbit crosses the celestial plane.

they do the radio beam fades away. There are about 20 known stellar mass black holes (found in X-ray binaries) with a relic population 3-10 times lower than the neutron stars, depending on the initial mass function (IMF) used to calculate them (see Fig. C.1). The fact that there exists this big difference in the predicted number of bodies due to the choice of IMF is what makes these so interesting to look at. If the population of relic black holes and neutron stars can be probed by Gaia it would mean that we constrain the top half of the IMF, where the different models differ the most (as seen in Fig. C.1 in the Appendix). Not only would this tell us about the massive star formation history of the Milky Way but it would also be useful for cosmology since the models of the early galaxies are based on the Milky Way.

Knowing the number of relic bodies in each population we can use this to estimate the average distance to either of the bodies. This is done by assuming that the bodies are homogeneously distributed in a cylinder which is 2 kpc thick and has a radius of 15 kpc. This assumption is made based on two things: the progenitor stars have to be very massive and thus are likely located near the Galactic plane, but when a star goes supernova the remain will receive a kick. Having a height of 2 kpc thick cylinders assures that these kicked bodies are included. This is also the scale height of the thick disk, which is the old stellar population of the Galaxy so to get the Brown Dwarfs accurately as well. The distance to the closest body from each population is then given roughly as:

$$R \approx \sqrt[3]{\frac{V}{N}} \tag{2.13}$$

Where V is the volume of the assumed cylinder and N the number of members in each population. For neutron stars we find $R_{NS} \approx 8 - 11$ pc and for black holes $R_{BH} \approx 14 - 24$ pc. These numbers are only meant to be used as a benchmark for when making rough approximations.

2.4.3 Relic brown dwarfs

Brown dwarfs have already been mentioned in the context that the Sun might have a binary companion brown dwarf but this is not the only way in which the brown dwarfs should be considered as there is a lot of them allover the Galaxy. Just as the heavy bodies they are also hard to detect since they are very faint from the beginning and then they cool and become even fainter. Obviously, unlike the neutron stars and black holes brown dwarfs are not very massive; which makes them worse candidates for lenses. However if we look at the Kroupa (2001) IMF we see that it predicts $\sim 10^{10}$ brown dwarfs in the Galaxy which means that they on average will be nearer than the heavy bodies so they are still viable candidates. Because as Eq. 3.1 shows the Einstein radius depends on both mass and distance and Eq. 2.9 shows that the deflection only depends on the Einstein radius and angular separation. Repeating the exact same procedure as before we get $R_{BD} \approx 5.2$ pc. A value comparable to the closest discovered brown dwarf, WISE 08550714 which is located at 2.2. pc (Luhman, 2014).

2.4.4 Intermediate mass black holes

The existence of intermediate mass black holes (IMBHs) has not yet been confirmed though there is some evidence pointing towards their existence. These include dynamical measurements of globular clusters (Noyola et al., 2010) or ultra-luminous X-ray sources in nearby galaxies (Farrell et al., 2009). Rashkov & Madau (2014) predict the number of IMBHs that could exist in the Milky Way and ends up with $70 - 2000$ distributed in the Halo. Them being so few makes the approximation made in Eq. 2.13 pointless, they should still be considered since the large concentrated mass makes them interesting objects for this work.

2.5 Mass determinations

Besides looking for invisible bodies, the effect of weak lensing can be used to weigh visible objects. Because if the position of the lens is known, the only free parameter which determines the magnitude of the lensing is the mass of the lens. Determining positions is exactly what Gaia does, which makes this test a viable thing to do with Gaia. Also, this test has two inherent advantages over the detection and determining the position and mass of invisible bodies. Firstly, only determining the mass and not the position at the same time makes it a lot easier to solve. Secondly, the need to find lensing events disappears because when Gaia measures the position of the lens it will also measure the position of all its neighbors. There are types of bodies which this method could be applied to are listed below:

Stars

Currently the only stars for which the mass can be directly measured is the Sun and eclipsing binaries. The mass determination of every other star is based on stellar evolution model or astroseismology which are all mostly based on the Sun. This makes the possibility of determining the masses of nearby stars important as it will help constrain the models used for mass determination.

Brown Dwarfs

The newly discovered brown dwarf mentioned in section 2.4.3 has been determined to have a mass of $3 - 10$ M_j and be $1 - 10$ Gyrs old (Trujillo & Sheppard, 2014). This large uncertainty comes from the fact that there exists a degeneracy between age and mass. The mass of the brown dwarf will determine the amount of energy it captures at its formation and the age will determine how much energy has been radiated away. Therefore being able to determine its mass in an independent manner would help further understand brown dwarfs.

Asteroids

Besides determining the position of stars, Gaia will determine the position of tens of thousands of solar system objects. For most of these objects (all except the planets, their moons and a few of the major asteroids) the masses are not well determined. Currently, their masses can be determined by, fitting their trajectory to the solar system potential, determining their topology by imaging them with a telescope and then by assuming some type of internal density or by visiting them with an orbiter. The estimates produced by the first two models do not produce accurate mass determinations and the last one is a very expensive and inefficient way of determining their masses. These types of bodies have very low masses, which at first makes it seem impossible for the method to work. However, they are located nearby, which means two things; their Einstein radius will still be non-negligible (for 10^{22} kg body at one AU, $\theta_E = 300\mu$as and they will also have a very large parallax motion which greatly increases the chance that they give a detectable deflection. A similar argument can be made for the more massive Kuiper belt objects.

Chapter 3

Using gravitational lensing

3.1 Estimating the detectability

The astrometric shift as described in Eq. 2.9 can be rewritten in a more convenient form (Gaudi & Bloom, 2005) as:

$$\Delta\theta = \frac{\theta_{sl}}{\left(\frac{\theta_{sl}}{\theta_E}\right)^2 + 2} \tag{3.1}$$

where θ_{sl} is the angular the separation between the source and lens, θ_E is the Einstein radius of the lens, given by Eq. 2.5 and $\Delta\theta$ corresponds to α, i.e. the deflection angle in Fig. 2.1. However in most cases the source will be significantly more distant than the lens meaning that the Einstein radius can be written as:

$$\theta_E \approx \sqrt{\frac{4G}{c^2}\frac{M}{d}} \tag{3.2}$$

Where d is the distance to the lens. Further, assuming that the average distance between source and lens is given by the average distance between stars which is given by dividing the angular area of the sky by the number of sources:

$$\sqrt{\frac{41253/10^8}{\pi}} \approx 40\text{as} \tag{3.3}$$

and that $\Delta\theta$ needs to be greater than 30 μas[1] an approximation can be made for the minimum size of the Einstein radius that the lens needs to have in order for it to give detectable deflections.

$$\frac{\theta_{sl}}{\left(\frac{\theta_{sl}}{\theta_E}\right)^2 + 2} = \Delta\theta \Rightarrow \theta_{sl} = \Delta\theta\left(\left(\frac{\theta_{sl}}{\theta_E}\right)^2 + 2\right) \tag{3.4}$$

Now, inserting the values of $\Delta\theta$ and θ_{sl} in arcseconds we get:

$$40 = 3\times10^{-5}\left(\left(\frac{40}{\theta_E}\right)^2 + 2\right) \Rightarrow 40 = 0.048/\theta_E^2 + 6\times10^{-5} \Rightarrow 40 \approx 0.048/\theta_E^2 \tag{3.5}$$

Rewriting this as an inequality we now find the minimum required Einstein radius that on average will be detected.

$$\theta_E^2 \geq \frac{0.048}{40} \Rightarrow \theta_E \geq 3.5 \text{ mas} \tag{3.6}$$

[1] Approximately the sensitivity of Gaia for the bright stars for a single set of measurements, i.e. 10 CCD crossings.

Meaning that every body with an Einstein radius greater than 3.5 mas in theory should give at least one detection. Using the approximative θ_E given in Eq. 3.2 we can plot the mass-distance relation:

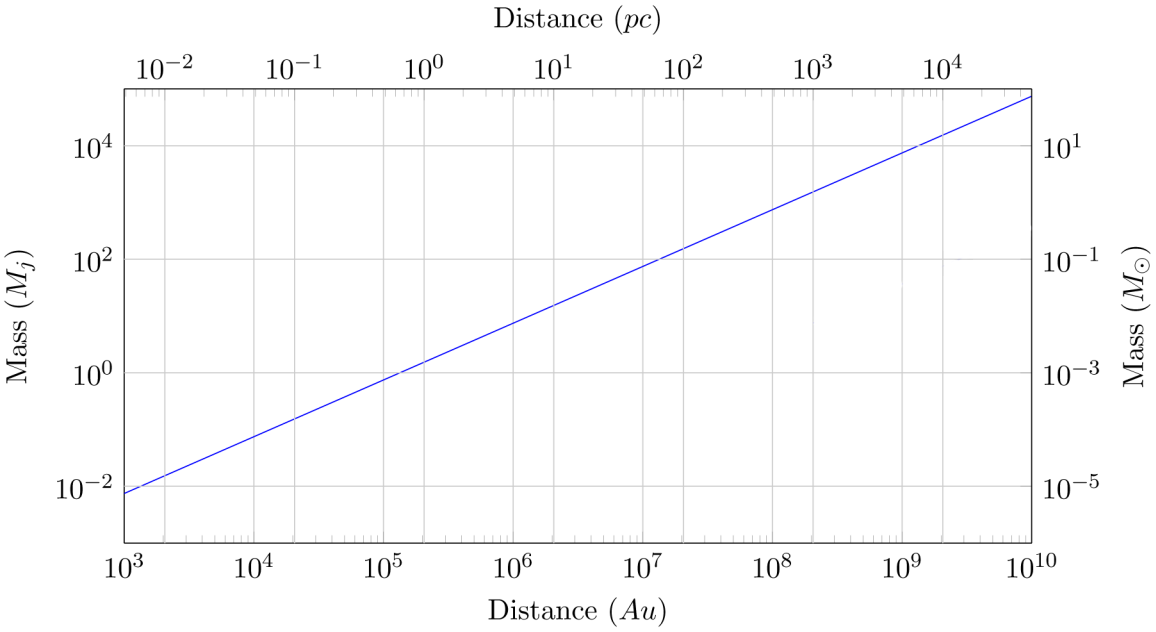

Figure 3.1: The plot shows at what distance a body of a given mass will have an Einstein radius of 3.5 mas and on average give a detectable deflection as shown in Eq. 3.6.

The assumptions made in order to get the prediction in Fig. 3.1 is rather simplistic and probably too optimistic which can be deduced by simply looking at the skymaps shown in Fig. 1.4. Not only that, but the area swept by the parallax motion will go down as the distance increases, meaning the scaling will not be as simple as it is assumed to be here. What this figure should be considered is a zero order approximation of what distance astrometric lensing events should be detectable by a body of a given mass.

3.2 Lensing model used in this project

We work with a simpler, geometrical model of general relativity, but this model must be equivalent with the Gaia relativistic model (GREM) shown in Appendix A, so the first thing to do is to show that we can rewrite A.8 as:

$$-\mathbf{n} = \left\langle -\sigma + \mathbf{r_{0L}} \frac{(1+\gamma)GM_L c^{-2}}{r_{oA}(r_{oA} - \sigma \cdot \mathbf{r_{0L}})} \right\rangle \tag{3.7}$$

What this equation shows is explained after Eq. 3.8 is presented as it is the same equation as the one above but using the vectors that will be used throughout this work. The nomenclature for gravitational lensing varies depending on which literature one looks at. So for the sake of clarity Fig. 3.2 and table 3.1 are included.

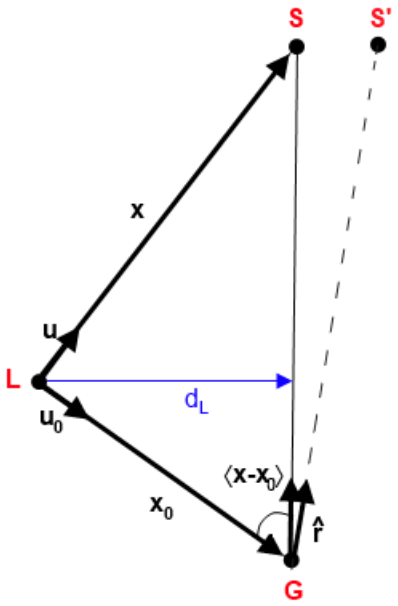

Figure 3.2: Gravitational lensing as described by Murray (1983). The black letters are the different vectors. The red letters denote the different objects, (G) Gaia, (L) Lens, (S) Source, (S') Apparent position of Source. d_L was added in the figure to help show the equivalence between this model and GREM.

Murray (1983)	Klioner (2008)	Lindegren (1992)	AGISLab
$\langle \mathbf{x} - \mathbf{x_0} \rangle$	$-\mathbf{k} \approx -\sigma$	$\bar{\mathbf{u}}$	$\bar{\mathbf{u}}$
$\hat{\mathbf{r}}$	$-\mathbf{n}$	$\hat{\mathbf{u}}$	$\hat{\mathbf{u}}$
$\mathbf{u_0}$	$\hat{\mathbf{r}}_{\mathbf{oA}}$	$\hat{\mathbf{h}}$	$\hat{\mathbf{r}} = \langle \mathbf{r} \rangle$
$\mathbf{x_0}$	$\mathbf{r}_{\mathbf{oA}}$	$\mathbf{h}$	$\mathbf{r}$
$\lvert\mathbf{x_0}\rvert$	r_{oA}	h	r
$\mathbf{u}$	N/A	N/A	N/A

Table 3.1: Comparison of literature

Using Table 3.1 we can write Eq. 3.7 as:

$$\hat{\mathbf{u}} = \left\langle \bar{\mathbf{u}} + \mathbf{r}\frac{(1+\gamma)GM_L c^{-2}}{r(r - \bar{\mathbf{u}} \cdot \mathbf{r})} \right\rangle \tag{3.8}$$

Before we move on, let us take a look at what this equation shows $\hat{\mathbf{u}}$ is a unit vector which gives the measured direction to a given source, $\bar{\mathbf{u}}$ is the so called proper direction to the source, i.e. where it would appear if it was not being lensed. The lensing is added to $\bar{\mathbf{u}}$ with $\mathbf{r}\frac{(1+\gamma)GM_L c^{-2}}{r(r-\bar{\mathbf{u}}\cdot\mathbf{r})}$ which gives the deflection from a lens with mass M located at $\mathbf{r}$. Now we want to show that this equals Eq. A.8. We start by looking at the vector $\mathbf{d_L}$:

$$\mathbf{d_L} = \sigma \times (\mathbf{r_{oA}} \times \sigma) = \bar{\mathbf{u}} \times (\mathbf{r} \times \bar{\mathbf{u}}) = \bar{\mathbf{u}} \cdot \bar{\mathbf{u}}\mathbf{r} - \bar{\mathbf{u}} \cdot \mathbf{r}\bar{\mathbf{u}} \tag{3.9}$$

since $\bar{\mathbf{u}}$ is a unit vector this equals:

$$\mathbf{d_L} = \mathbf{r} - \bar{\mathbf{u}} \cdot \mathbf{r}\bar{\mathbf{u}} = \mathbf{r} - \bar{\mathbf{u}}\bar{\mathbf{u}} \cdot \mathbf{r} = \mathbf{r} - \bar{\mathbf{u}}(\bar{\mathbf{u}} \cdot \mathbf{r}) \tag{3.10}$$

Here we can see that $\mathbf{d_L} \cdot \bar{\mathbf{u}} = \mathbf{r} \cdot \bar{\mathbf{u}} - (\bar{\mathbf{u}} \cdot \bar{\mathbf{u}})(\bar{\mathbf{u}} \cdot \mathbf{r}) = 0$, it follows that $\mathbf{d_L} \perp \bar{\mathbf{u}}$. This means that $\bar{\mathbf{u}} + \mathbf{d_L} \cdot k$ where $k > 0$ cannot be a unit vector, which is what we have constructed $\hat{\mathbf{u}}$ to be.
Now, if we look at Eq. A.8 we see that

$$\delta\sigma = \hat{\mathbf{u}} - \bar{\mathbf{u}}. \tag{3.11}$$

which we now can rewrite as, using table 3.1

$$\hat{\mathbf{u}} = \bar{\mathbf{u}} + \mathbf{d_L}\frac{GM_L c^{-2}}{|\mathbf{d_L}|^2}(1 - \bar{\mathbf{u}} \cdot \mathbf{r}) \tag{3.12}$$

Since we just showed that this cannot equal unity, it means that the two models will not be strictly equivalent. However, to first order they are, as shown below. We introduce the parameter ϵ:

$$\epsilon = \frac{(1+\gamma)GM_L c^{-2}}{r(r + \mathbf{r} \cdot \bar{\mathbf{u}})} \tag{3.13}$$

Which means that we can rewrite Eq. 3.8:

$$\hat{\mathbf{u}} = \langle \bar{\mathbf{u}} + \mathbf{r}\epsilon \rangle = \frac{\bar{\mathbf{u}} + \mathbf{r}\epsilon}{|\bar{\mathbf{u}} + \mathbf{r}\epsilon|} = \frac{\bar{\mathbf{u}} + \mathbf{r}\epsilon}{\sqrt{(\bar{\mathbf{u}} + \mathbf{r}\epsilon) \cdot (\bar{\mathbf{u}} + \mathbf{r}\epsilon)}} \tag{3.14}$$

Then we do some approximations in the denominator, we say that:

$$(\bar{\mathbf{u}} + \mathbf{r}\epsilon) \cdot (\bar{\mathbf{u}} + \mathbf{r}\epsilon) = 1 + 2\epsilon\bar{\mathbf{u}} \cdot \mathbf{r} + \mathcal{O}(\epsilon^2) \tag{3.15}$$

An inverse square root can be Taylor expanded as:

$$\sqrt{}^{-1} \approx 1 - \epsilon\bar{\mathbf{u}} \cdot \mathbf{r} + \mathcal{O}(\epsilon^2) \tag{3.16}$$

This means that we can write $\hat{\mathbf{u}}$ as:

$$\hat{\mathbf{u}} = \bar{\mathbf{u}} + (\mathbf{r} - \bar{\mathbf{u}}(\mathbf{r} \cdot \hat{\mathbf{u}}))\epsilon + \mathcal{O}(\epsilon^2) \tag{3.17}$$

Now it is easy to show that this model, to the first order, is strictly equal to GREM by rewriting Eq. 3.12 using Eq. 3.10:

$$|\mathbf{d_L}|^2 = \mathbf{d_L} \cdot \mathbf{d_L} = |\mathbf{r}|^2 - 2(\bar{\mathbf{u}} \cdot \mathbf{r})^2 + (\bar{\mathbf{u}}\bar{\mathbf{u}})(\bar{\mathbf{u}} \cdot \mathbf{r})^2 = r^2(1 - (\bar{\mathbf{u}} \cdot \hat{\mathbf{r}})^2) \tag{3.18}$$

Since $\mathbf{r} = \hat{\mathbf{r}}r$ Eq. 3.12 becomes:

$$\hat{\mathbf{u}} = \bar{\mathbf{u}} + (\mathbf{r} - \bar{\mathbf{u}}(\mathbf{r}\cdot\bar{\mathbf{u}}))\frac{GM_L c^{-2}}{r^2(1 - (\bar{\mathbf{u}} \cdot \mathbf{r})^2)}(1 - \bar{\mathbf{u}}\cdot\mathbf{r}) = \bar{\mathbf{u}} + (\mathbf{r} - \bar{\mathbf{u}}(\mathbf{r}\cdot\bar{\mathbf{u}}))\frac{GM_L c^{-2}}{r^2(1 + (\bar{\mathbf{u}} \cdot \hat{\mathbf{r}}))} = \bar{\mathbf{u}} + (\mathbf{r} - \bar{\mathbf{u}}(\mathbf{r}\cdot\bar{\mathbf{u}}))\epsilon \tag{3.19}$$

QED. We have thus shown that the geometric model used in this work is equivalent to GRM to an accuracy on the order $\mathcal{O}(\epsilon)$.

3.2.1 Deriving the partial derivatives

In order fit the model to the observation and recover the lens parameters (M_L, r_x, r_y, r_z), we need the partial derivatives of $\hat{\mathbf{u}}$ with respect to them. We use the approximative $\hat{\mathbf{u}}$ given in Eq. 3.17. The derivative with respect to mass is straight forward to calculate, however the r-derivatives are calculated component wise as shown below:

$$\frac{\partial \hat{u}_j}{\partial r_i} \tag{3.20}$$

Due to symmetry, all the r-derivatives of $\hat{\mathbf{u}}$ will be the same. The derivative will be a vector of which two of the components will be the same. So we only need to look at the two cases, case 1 when $i \neq j$ and case 2 when they are equal.
We can view $\hat{\mathbf{u}}$ as one function f divided by another function g:

$$\hat{\mathbf{u}} = \frac{f}{g} \tag{3.21}$$

so the derivative is then given by:

$$\frac{\partial \hat{u}}{\partial r} = \frac{f'g - g'f}{g^2} \tag{3.22}$$

Where

$$f = \frac{GM_L(1+\gamma)}{c^2}\left(\mathbf{r} - \bar{\mathbf{u}}(\bar{\mathbf{u}} \cdot \mathbf{r})\right) \tag{3.23}$$

and

$$g = r(r + \mathbf{r} \cdot \bar{\mathbf{u}}) \tag{3.24}$$

Note that g is a scalar and the derivative will be the same in both cases. The derivatives of are:
Case 1

$$f' = -\frac{GM_L(1+\gamma)}{c^2}(u_i u_j) \tag{3.25}$$

$$g' = \frac{r_i}{r}(r + \bar{\mathbf{u}} \cdot \mathbf{r}) + r(\frac{r_i}{r} + u_i) \tag{3.26}$$

Case 2

$$f' = \frac{GM_L(1+\gamma)}{c^2}(1 - u_j^2) \tag{3.27}$$

$$g' = \frac{r_j}{r}(r + \bar{\mathbf{u}} \cdot \mathbf{r}) + r(\frac{r_j}{r} + u_j) \tag{3.28}$$

Now by combining these we get:

$$\frac{\partial \hat{u}_j}{\partial r_i} = \frac{GM_L(1+\gamma)}{c^2}\frac{-(u_i u_j)r(r + \mathbf{r} \cdot \bar{\mathbf{u}}) - (r_j - u_j(\bar{\mathbf{u}} \cdot \mathbf{r}))\left(\frac{r_j}{r}(r + \bar{\mathbf{u}} \cdot \mathbf{r}) + r(\frac{r_j}{r} + u_j)\right)}{r^2(r + \mathbf{r} \cdot \bar{\mathbf{u}})^2} \tag{3.29}$$

$$\frac{\partial \hat{u}_j}{\partial r_j} = \frac{GM_L(1+\gamma)}{c^2}\frac{(1 - u_j^2)r(r + \mathbf{r} \cdot \bar{\mathbf{u}}) - (r_j - u_j(\bar{\mathbf{u}} \cdot \mathbf{r}))\left(\frac{r_j}{r}(r + \bar{\mathbf{u}} \cdot \mathbf{r}) + r(\frac{r_j}{r} + u_j)\right)}{r^2(r + \bar{\mathbf{u}} \cdot \mathbf{r})^2} \tag{3.30}$$

Of course the mass derivative is also needed, but that is trivially obtained as:

$$\frac{\partial \hat{u}}{\partial M_L} = \frac{G(1+\gamma)}{c^2}\frac{\mathbf{r} - \bar{\mathbf{u}}(\bar{\mathbf{u}} \cdot \mathbf{r})}{r(r + \bar{\mathbf{u}} \cdot \mathbf{r})} \tag{3.31}$$

3.2.2 Testing the partial derivatives

Once the derivatives had been obtained two tests were preformed, the first of which was to test how the approximation propagated through to the derivative with regards to ϵ. We used Mathematica to take the analytical derivative of $\hat{\mathbf{u}}$ (which is a horrendous expression) and determined its numerical value for randomly selected vectors $\bar{\mathbf{u}}$ and $\mathbf{r}$. For every generated analytical value from the approximation was also generated, this was done for a range ϵ. What we found is shown in Fig. 3.3

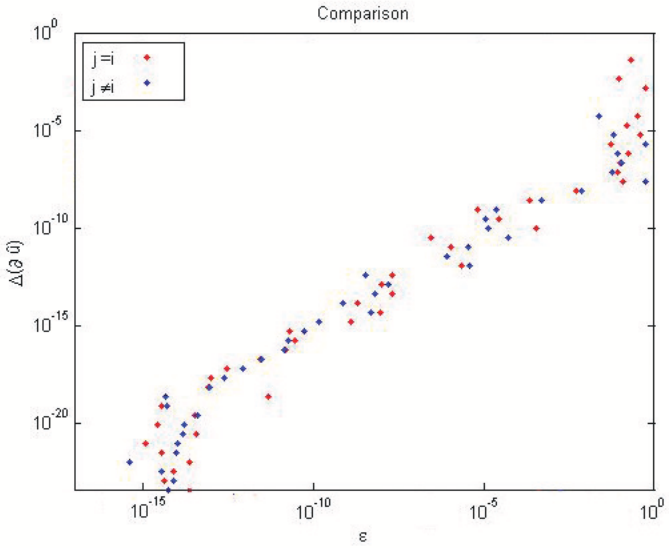

Figure 3.3: The plot shows $\Delta\partial\hat{\mathbf{u}}$, which is the absolute difference between the analytical and numerical derivative plotted in a log-log scale against the value of ϵ. It has a slope of 1, which means that $\Delta\partial\hat{\mathbf{u}} \propto \epsilon$. This means that the accuracy of the approximative derivative is the same as the accuracy of the deflection model, meaning we do not lose any information by utilizing it.

To preform the second test, a lens had to be implemented in AGISLab. Since a deflection equation already existed for Solar system bodies, this code was modified to work for an arbitrary lens. Once this was implemented, the validity of the partial derivatives could be tested using a simple central difference method. The method was set up in such a manner that for each of the partial derivatives being tested three identical observations were generated but the parameter of the lens being tested was varied for each observation. This perturbs the three different source directions differently, this perturbation can be used to take the central difference. Preforming this test we found a four digit accuracy which is what we expected for a first order central difference method.

Chapter 4

Results

Simulation setup

Once the partial derivatives of the lens equation had been derived and tested (as described in the previous chapter) they were implemented as part of the global block in the source direction calculation.

This means that the algorithm can attempt to recover the lens parameters whilst doing the optimization of the stellar parameters. It does this by taking the true (input) values of the lens parameters and then using them in the deflection equation (Eq. 3.8) to apply a perturbation to every the observation of each source. Then, the update algorithm will use the partial derivatives (Eqs. 3.29, 3.30, 3.31) to attempt to reduce the observational residuals as much as possible. This will be when the running (optimized) values are close to the true values. The entire perturbation will not be recovered as there is observation noise to realistically simulate the real Gaia mission, (de Bruijne, 2009).

The sources in the simulation are all set up to be of magnitude 13. What this means for the purpose of this simulation is simply that this is within the region where Gaia is as most accurate, i.e. the stellar parameters will be determined to an accuracy of $\sim 8\mu as$. At this magnitude each of CCDs are accurate to $\sim 100\mu as$, however in each observation the source crosses 10 CCDs. Combining the 10 crossings with the astrometric solution leads to an accuracy of $\sim 100/\sqrt{10} \approx 30\mu as$, combining the measurements during the span of the mission further increases the accuracy. It is the astrometric solution which combines the multiple observations which makes Gaia achieve the accuracy it does. This is reflected in the simulation by the adding random noise to the observations.

To simulate the high source density observed by Gaia a simple method was implemented which placed all of the sources near the lens in a small circular container because that is where the effect is greatest. The reason for this is that at that small radius is the place where the induced astrometric shift would be most significant (as shown in Fig. 4.5). Firstly, the source density was set as $10^8/41253 = 2424\ \text{deg}^{-2} = \hat{\rho}$, which is simply the number of square degrees in the sky[1] divided by 10% of sources observed by Gaia which we assume to be the number of sources to have its astrometric parameters determined to an accuracy equivalent of a 13 mag source. The source distribution is however far from homogeneous on the sky so $\hat{\rho}$ was only used as a reference and for tests in the beginning. In the later simulations three different densities were used: 2000 deg^{-2}, 10000 deg^{-2} and 30000 deg^{-2} .

When setting up the simulation there are a few settings that can be turned on or off that are not

[1]The number comes from the area of the surface of a unit sphere, 4π square radians converted to square degrees

of direct interest for our testing. The three different settings considered here are the source errors induced by the attitude (uncertainty in the pointing of Gaia, "attitude noise") and the random noise mentioned previously. Also of interest is the need to solve for the attitude and source parameters or whether the simulation can simply start from the true values. The effect of turning off errors is interesting because it allows for the running of simulations in which the only uncertainty in the astrometric parameters come from the lens, which means that one does not have to be concerned with whether the lensing signal is sufficiently strong and can test the fitting without considering this. Being able to turn off initial source errors without affecting the simulation speeds up the simulation by not having to wait for the parameters to converge. Being able to turn off the attitude solution greatly speeds up the simulation because it allows us to turn of an entire block as described in section 1.3.1 and it allows to only include the sources in the small circular container mentioned in the previous paragraph and still attain a good solution.[2]

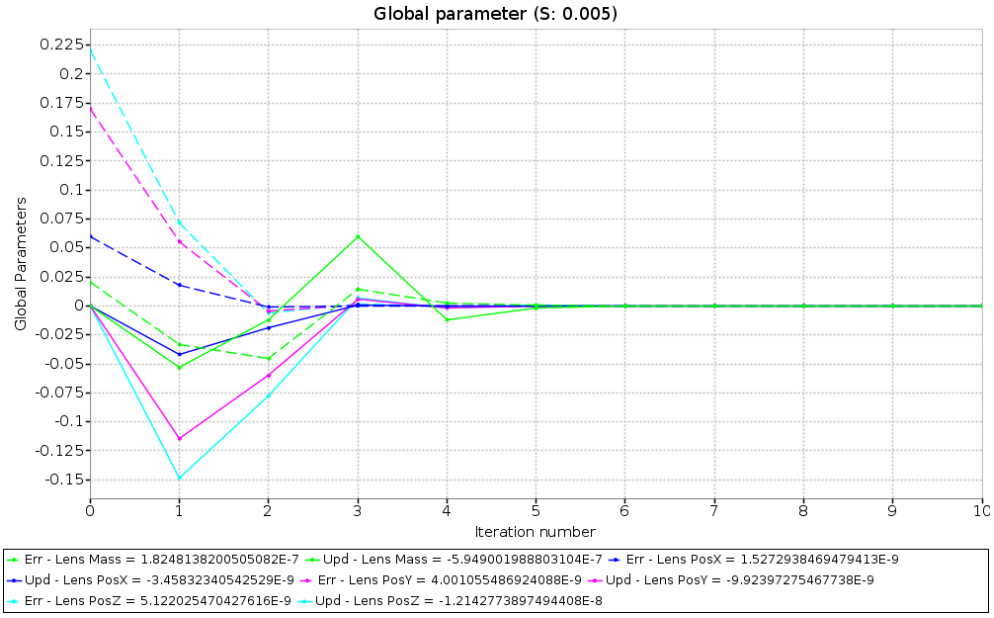

Figure 4.1: The figure above shows the convergence of the global parameters, which are M_L, x_L, y_L, and z_L with x, y, z being the BCRS position of the lens. The true values of these parameters are: $M_L = 1.25 M_J$, $x = 6$ AU, $y = 17$ AU and $z = 22$ AU. and the initial errors are: $M_L = 0.02 M_J$, $x = 0.06$ AU, $y = 0.17$ AU and $z = 0.22$ AU or 1% for distances and a bit more for the mass. The dashed lines in the figure show the value of the error for each parameter and the solid lines show the update in each parameter. The S at the top of the figure is the scale factor of the simulation, with $S = 1$ meaning a full attitude fit and the simulation uses 5 000 sources. The figure here shows that the solution converges easily, after only 5 iterations.

Figure 4.1 shows a run where the initial source error is set to zero, likewise is the initial attitude error. There is also no source nor attitude noise. This means that the only error in the source parameters arise from the lens. Which means that Fig. 4.1 shows the most efficient, fastest and accurate simulation that can be done. The following three figures show simulations where the initial source error is turned on, initial source error and noise is turned on, source errors on and attitude being solved for.

[2]In order to properly model the pointing of the spacecraft one would need to populate the entire celestial sphere with sources when doing the solution.

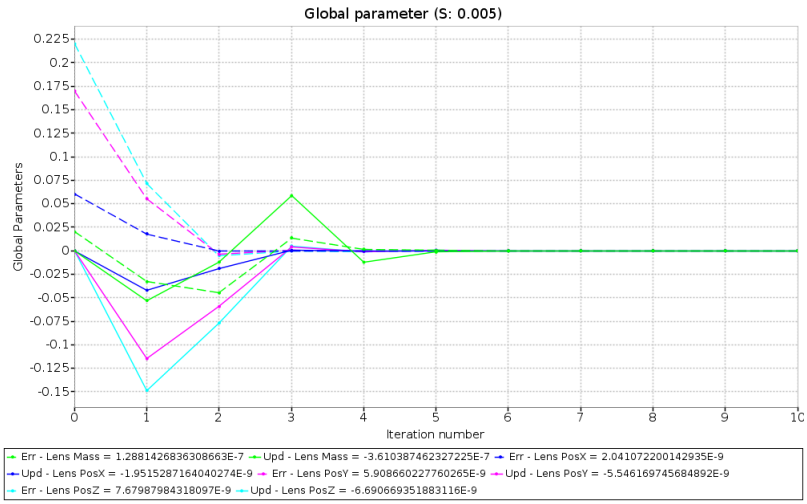

Figure 4.2: The panels show the convergence of a run with initial source errors of 100 mas, but no attitude nor source noise.

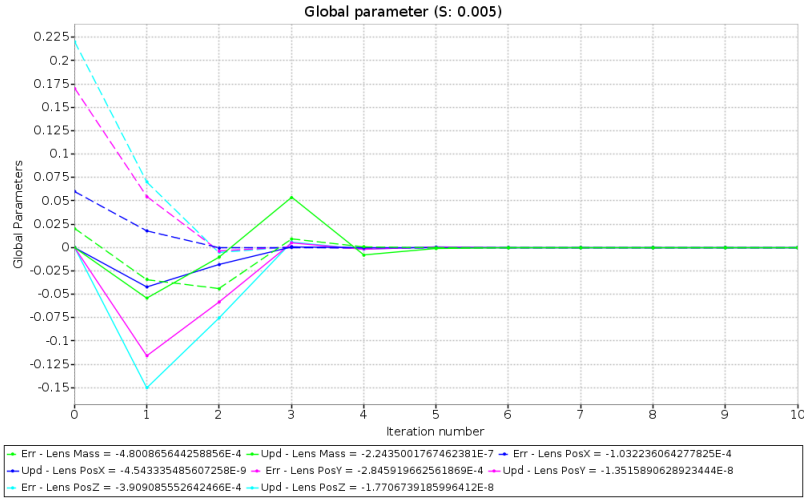

Figure 4.3: The panels show the convergence of a run with initial source errors of 100 mas, and standard source noise and no attitude noise

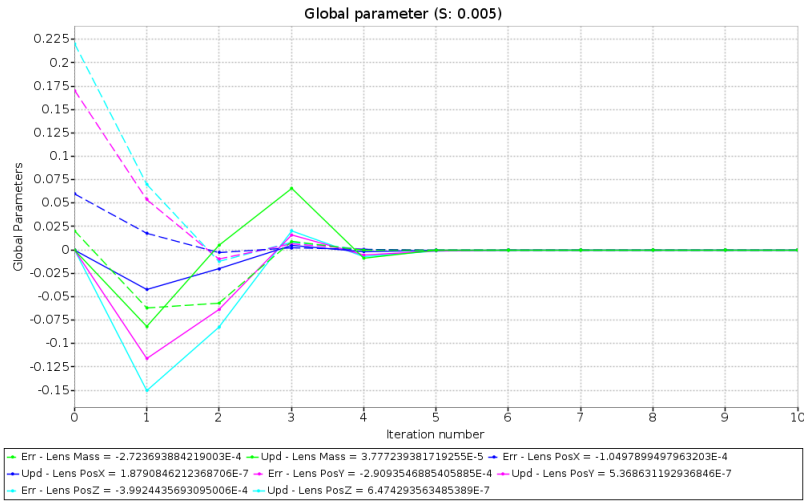

Figure 4.4: The panels show the convergence of a run with initial source errors of 100 mas, and standard source noise and attitude update with initial attitude error of 100 μas resulting in final attitude noise of ~ 10 μas

The four plots above being virtually identical means that the aforementioned properties can be toggled either way and the simulation will be reliable nonetheless. Most important of this is the fact that solving for the attitude does not affect the solution, because it allows us to: 1) Assume the attitude to be known and not solve for it, which greatly increases the speed of the solution and 2) Only use the small circular source container in the line of sight of the lens that was mentioned before.

4.1 Initial Simulations

Detectability

The first thing that needs to be determined is what is meant by detecting a body. How do we see the body in the data? As discussed previously, the bending of light will depend on the angular separation between lens and source. Since the parallax of the lens will be different than the stars it is lensing, the lensing magnitude will vary with each observation. This will result in having unexpectedly large observational residuals for certain sources, the observational residuals are simply a measure of how good a fit of parameters to a model is. The lens will give rise to specific patterns in the residuals, which is what we are looking for in the data. In this work we have chosen a Gaussian representation called Gaussian goodness of fit (henceforth, Gaussian GoF) for the residuals, the Gaussian GoF is given by first looking at the sum of squared residuals:

$$\text{ssr} = \sum_{i}^{N} \frac{(x_{i,\text{obs}} - x_{i,\text{model}})^2}{\sigma_i^2} \tag{4.1}$$

The expected value of the ssr is ν, where ν = number of degrees of freedom ($N_{\text{obs}} - N_{\text{par}}$ where $N_{\text{par}} = 5$) and the expected standard deviation is $\sqrt{2\nu}$. The Gaussian GoF is then calculated from this approximately as[3]

$$\text{GoF} = \frac{(\text{ssr} - \nu)}{\sqrt{2\nu}} \tag{4.2}$$

[3]The actual calculation is more complex than shown in Eq. 4.2, it involves some integral transformations which are numerically solved using the error function. The solution in the end is however very close to Eq. 4.2

The Gaussian GoF is expected to be Gaussian with zero mean and unit standard deviation. What the Gaussian GoF gives is the probability of a data point randomly having the value that it has (probability given by a $N(0,1)$ normal distribution). Figure 4.5 shows the Gaussian GoF of each source plotted on the sky from a simulation perturbed by a lens.

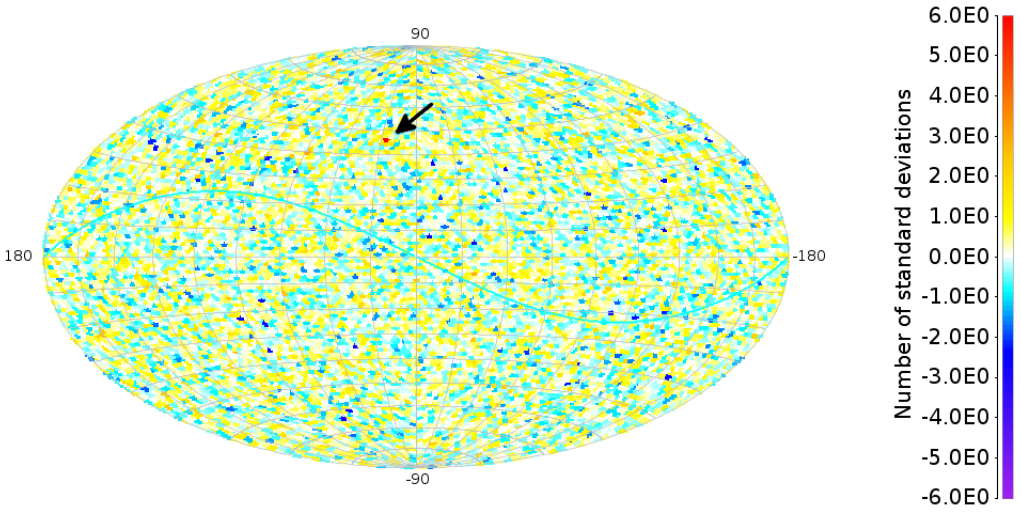

Figure 4.5: The figure shows the Gaussian GoF for the sources when having a the simulation setup described for the previous simulations but not removing the effect of the lens. The figure shows that there is a strong, $> 6\sigma$ signal that something is not as it should be, such a strong signal is expected for such a massive body inside the Solar system. Two things should however be noted, the signal is averaged over pixel density in this plot, so the area in which the effect of the lens appears is larger because more stars have been placed in that line of sight. Also, the code does not return values greater than $\sim 6\sigma$, it instead returns infinities because the transformation from ssr to Gaussian GoF involves putting the ssr in an exponent which in some cases can return values too large for the code to handle so it puts them to be infinite. Thusly all the sources that get an infinite GoF have their GoF set to equal 6

Zooming in on the area of the sky where the lens is located a particular pattern appears in the residuals, the figure below shows three different cases, the first one being 90° relative to the ecliptic, second one 45° and the third in the ecliptic.

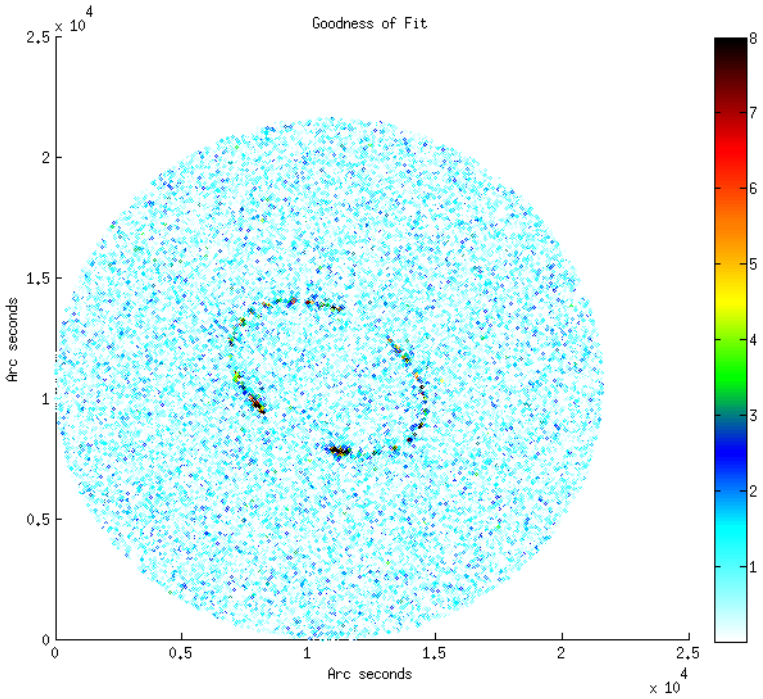

Figure 4.6: The figure above shows a field of sources being lensed by a Jupiter-mass body located at 50 AU, 45° relative to the ecliptic. Each source has been given a color corresponding to their Gaussian GoF which means that the colors show how perturbed the astrometric parameters for each source are.

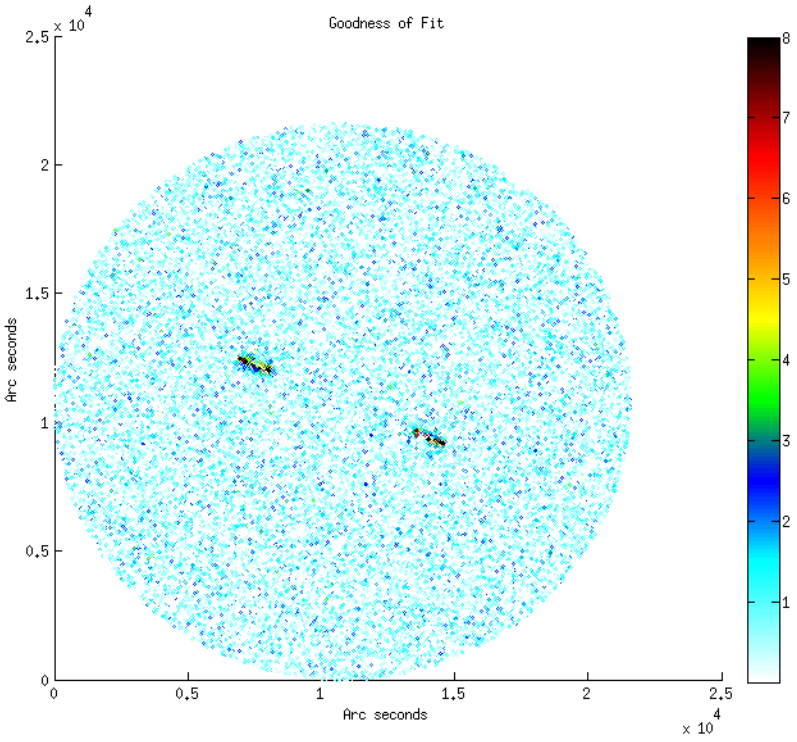

Figure 4.7: The figure above shows a field of sources being lensed by a Jupiter-mass body located at 50 AU in the ecliptic. Each source has been given a color corresponding to their Gaussian GoF which means that the colors show how perturbed the astrometric parameters for each source are

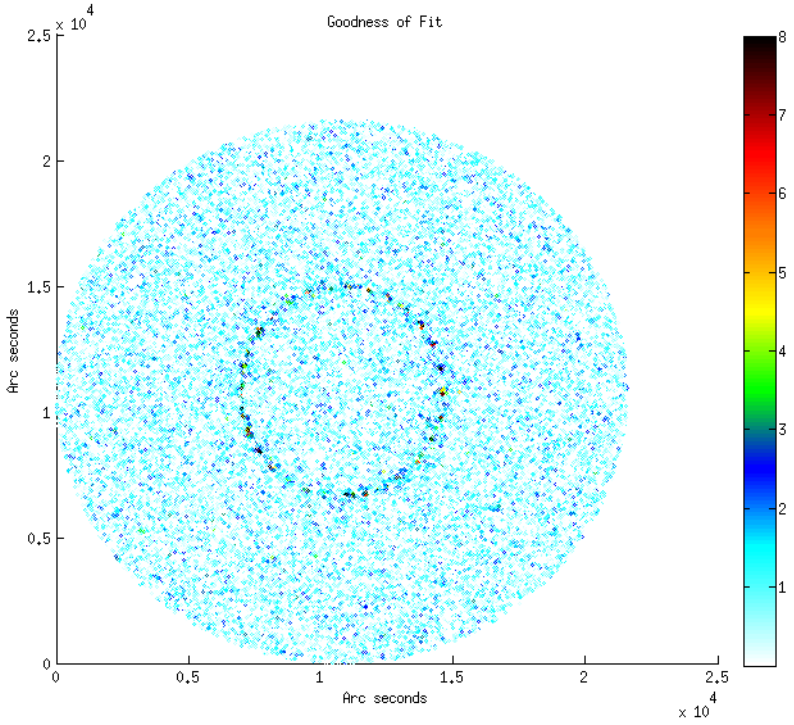

Figure 4.8: The figure above shows a field of sources being lensed by a Jupiter-mass body located at 50 AU, 90° relative to the ecliptic. Each source has been given a color corresponding to their Gaussian GoF which means that the colors show how perturbed the astrometric parameters for each source are.

The figure shows the residuals of a Jupiter-mass planet at 50 AU. The pattern seen in the residuals is the parallax motion of the lens. A symmetry appears in both Fig. 4.6 and 4.7 in that the sources in the middle of the ellipse appear not to be as perturbed. This is because on the sides of the ellipse is where the lens will be spend most of its time as it is there it moves 'inwards" and 'outwards' in the projection. Also, it will spend an equal amount of time on each side of the unperturbed sources which results in them being perturbed in the exact opposite direction an equal amount of time; resulting in their mean positions being well defined and close to their true positions. This pattern will however not be seen for lenses that have a small parallax, as there will not be enough stars that are lensed for the pattern to appear.

Another interesting thing this simulation shows is what happens to the parallax errors, Fig. 4.9 shows the parallax error for the same run as Fig. 4.6.

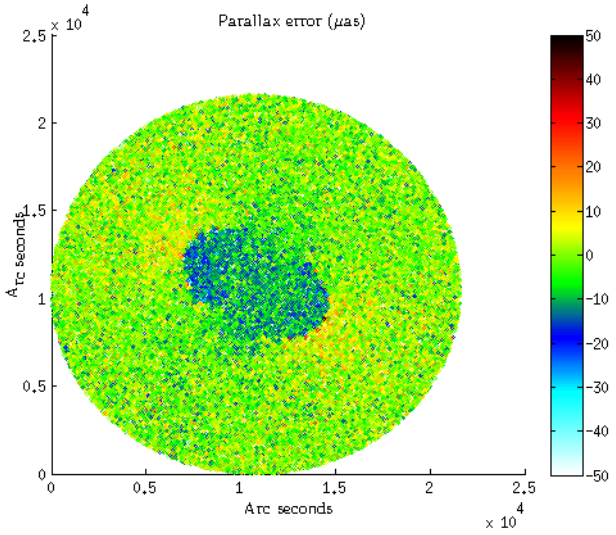

Figure 4.9: The error in parallax induced by a Jupiter-mass body located at 50 AU, 45° relative to the ecliptic.

Of course, the error presented in this way will never be available since the true value is never known. However, knowing the parallax error can still be useful as Gaia will observe some so called zero-parallax sources, such as galaxies, quasars and (very) distant halo stars. Because when the data is reduced, AGIS will still fit a parallax to these sources, and these parallaxes will be distributed around zero. This means that if a negative shift is seen in the parallax-distribution of these objects in a certain region of the sky, it could indicate the presence of a lens. Interestingly the negative shift is only seen inside the ellipse drawn by the parallax motion which means that this way of finding bodies will be a lot more useful for nearby bodies as the probability of having a zero-parallax object inside the ellipse will be significantly higher. This effect is explained and discussed in Section 4.3.4 ("Zero-parallax objects").

Finally, in the initial detectability simulations we also notice that it is nearly impossible to detect nearby bodies that are not very massive. This is likely due to a dilution of lensing events and is discussed in detail in the Section 4.3.1 ("Detecting Solar system objects"). The effect is also shown in the Fig. 4.10:

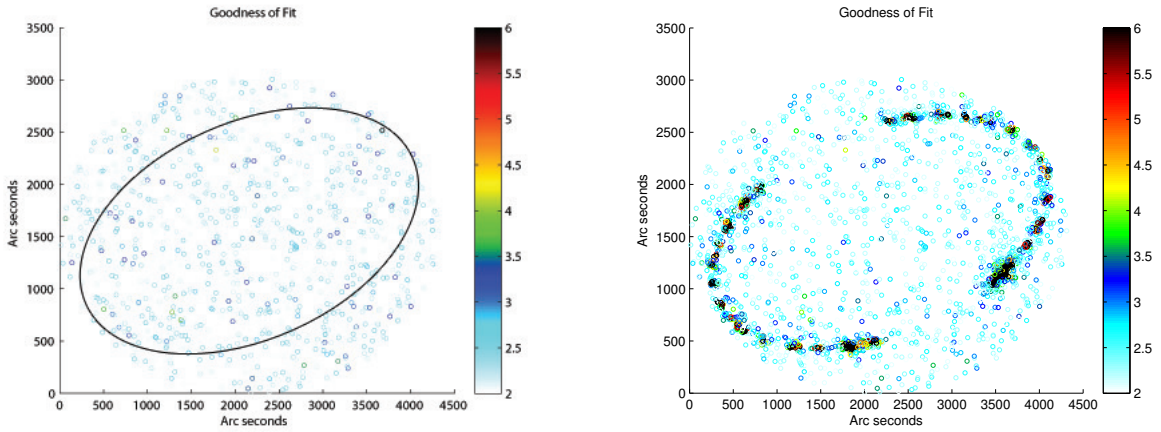

Figure 4.10: The left panel shows the Gaussian GoF of the stars being perturbed by a Neptune mass body at 100 AU whereas the right panel shows a Jupiter mass body also at 100 AU. The parallax motion of the Jupiter mass body is clearly visible in the observational residuals and around the outline of how the lens is supposed to move one can barely make out a similar pattern in the left panel. It would however be nearly impossible to infer the existence of a lens in the left panel without knowing exactly where to look.

Determining all the lens parameters

When checking the different simulation setups when doing the initial simulations we saw that it was quite hard to find fits which converged correctly. Figure 4.1 shown before shows an attempt to fit the lensing model to a 1.2 Jupiter-mass planet at $\sim$ 30 AU, which should be easy since the signal from the lens is very strong. However, when testing we saw that achieving convergence is hard even without source errors. Figure 4.11 is one example of how a slight change in the simulation setup can affect the outcome, in this case the initial errors were doubled from 1% to 2% and it did not converge.

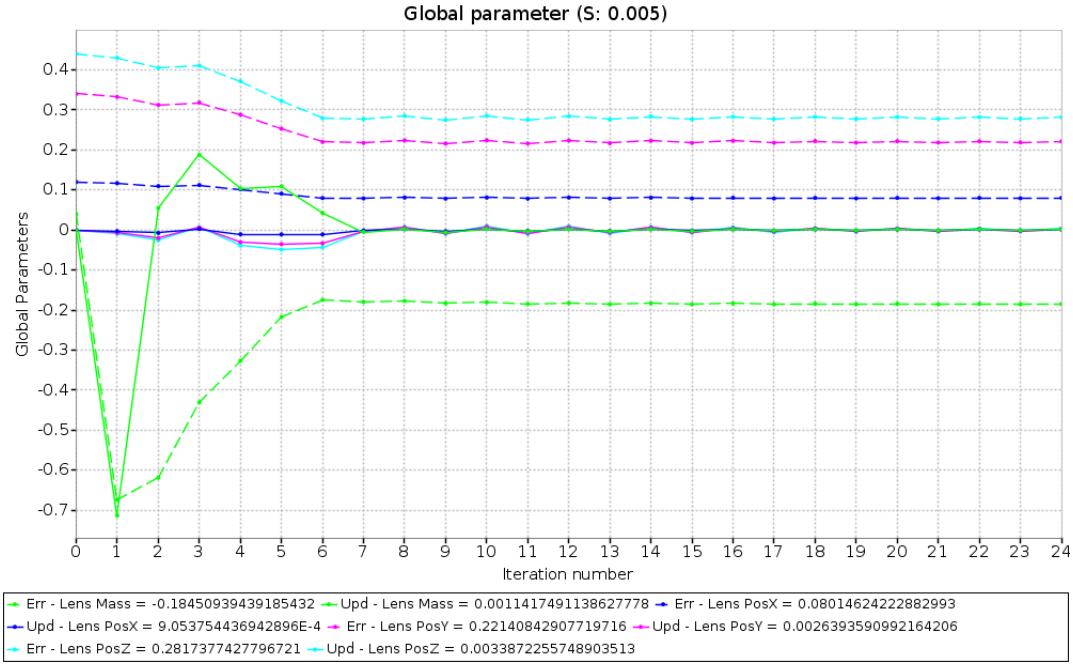

Figure 4.11: The figure shows a simulation set up as and with the exact same parameters and conditions as the simulation in Fig. 4.1 but with doubled initial errors and in this case the algorithm cannot find the correct fit.

Another thing that was found which makes the algorithm to fail to converge is shown below, all that was changed in this simulation was that the scaling parameter S was set to 0.025 instead of 0.005.

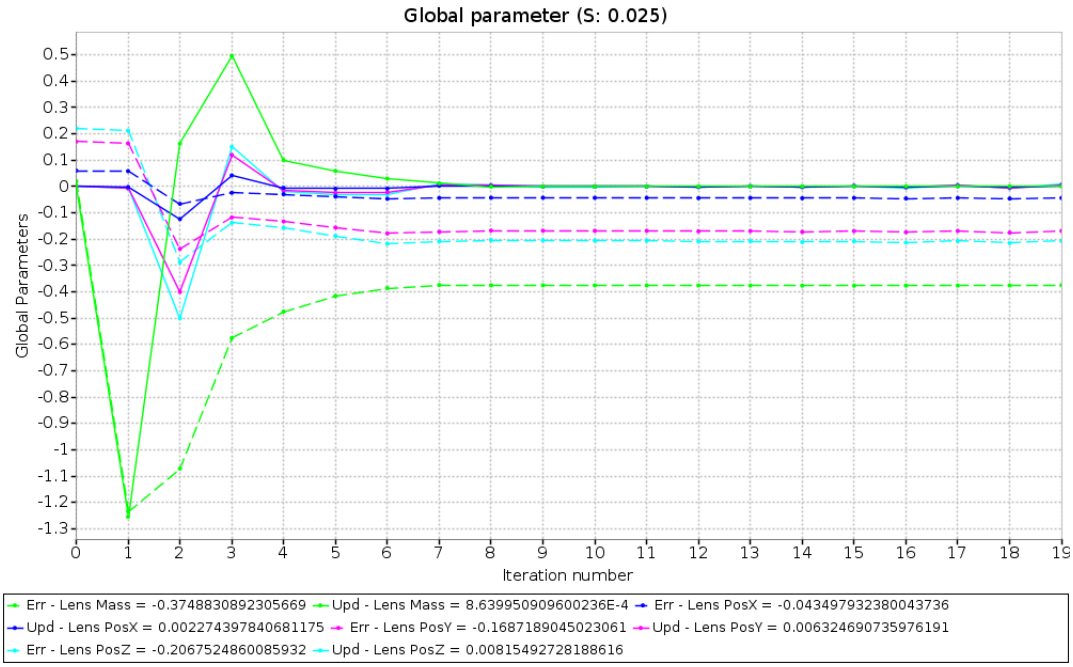

Figure 4.12: The figure shows a simulation set up as and with the exact same parameters and conditions as the simulation in Fig. 4.1 but with a scale factor of 0.025 instead of 0.005 and in this case the algorithm cannot find the correct solution.

The reason for this behavior can be seen by looking at Eqs. 3.29, 3.30, 3.31, the system of equations is highly non-linear, i.e. the update in each of the components of will be dependent on the other components. This means that it will be hard for an algorithm to find its way out of a local minimum, which is problematic because we know there to be many degeneracies in the problem (can be seen easily in Eq. 2.6 which shows that $\theta_E \propto M/d$). The simulations also showed that the algorithm only finds the correct fit for the position if the relative initial errors are equal, i.e.

$$\frac{r_{x,\text{error}}}{r_x} = \frac{r_{y,\text{error}}}{r_y} = \frac{r_{z,\text{error}}}{r_z} \tag{4.3}$$

and when this is the case the simulations show that the relative updates are also equal. What this means in physical terms is that the algorithm is able to move the lens back and forward in the radial direction (change all components of a vector relatively equally and only the length of the vector changes) yet it has a hard time moving the lens transversely. The only plausible explanation for this is the non-linearity of the problem and looking at Fig. 4.13 further shows that the non-linearity is the problem. Because in this figure the initial value of the position is off-center (the algorithm has to move the lens in the transverse direction) and also so small that non-linear effects should not matter, and in this case it converges in only six iterations.

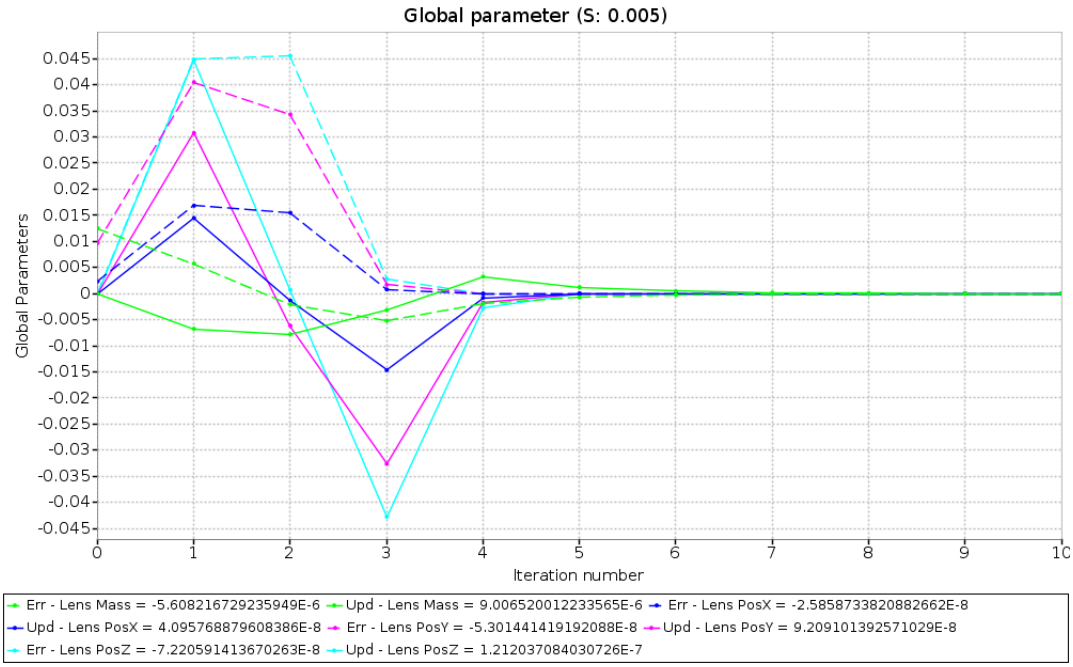

Figure 4.13: The figure shows a run in which the initial values are so small that non-linear effects do not matter.

Besides this, the denominator of each positional derivative contains a r^4-term which means that the initial errors will be magnified as they propagate through the algorithm. Combining these facts leads to the conclusion that that when the updates in the fitting go towards zero, it will be impossible to determine whether it is in the global minimum or a nearby local minimum.

After thoroughly testing every other possibility we could think of we come to the conclusion that this method of determining positions and masses of bodies is not feasible, since the initial guess has to be so near the true values for the algorithm to have a chance of convergence. And all the tests are consistent with non-linearity being a large part of the problem.

4.1.1 Mass determinations

The discussion regarding the simulation setup in the previous section is also valid here. Yet the problems with non-linearity are not expected to arise because unlike in the previous test this is only solving for a single parameter using a single equation. The linearity can also easily be demonstrated by setting up a run which starts far away from its true value. Solving for the mass of the lens in the previous section (Jupiter located at ∼30 AU) with an initial guess of 11 Jupiter-masses the fitting is shown in 4.14.

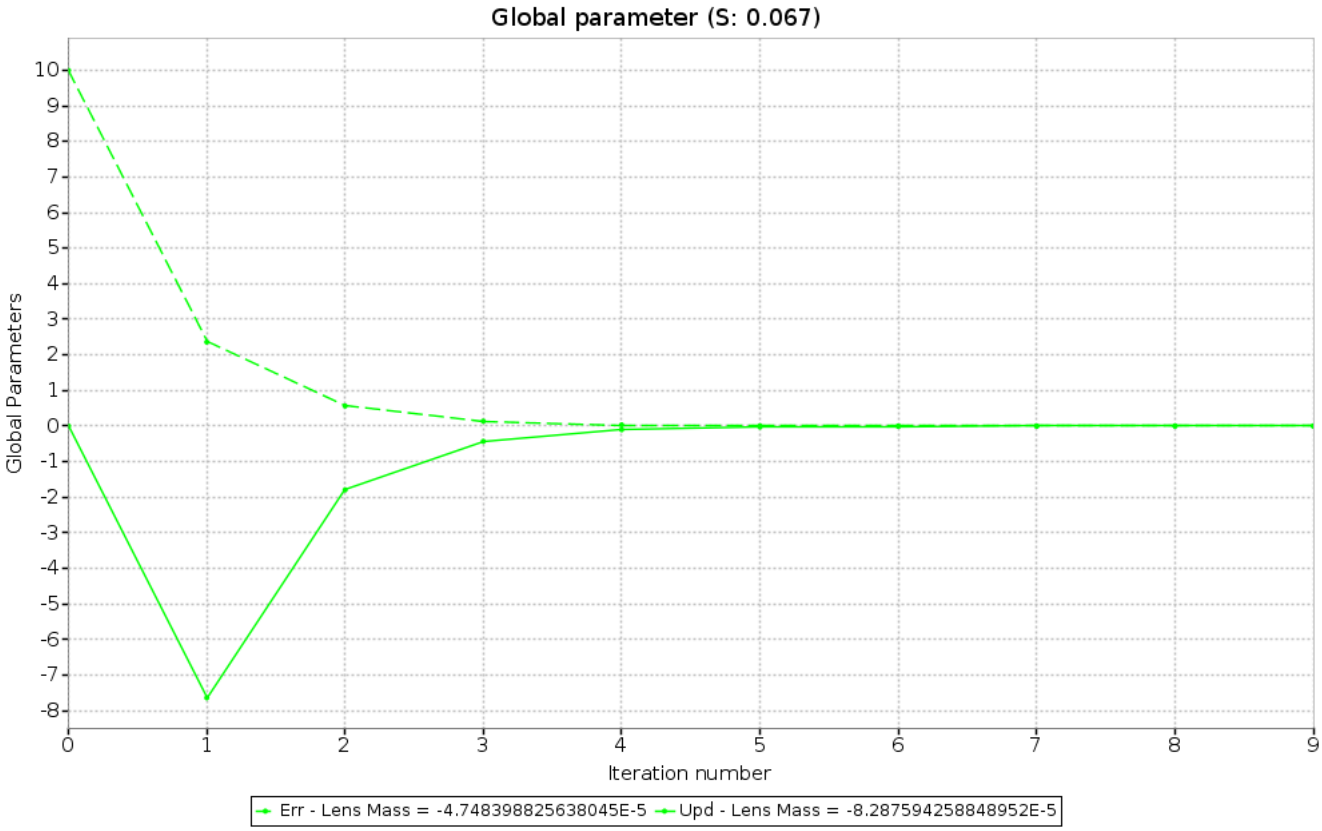

Figure 4.14: Convergence plot when solving for a Jupiter mass planet with known position, located at 30 AU and an initial guess of 11 Jupiter-masses.

As expected, the algorithm behaves well. Not only was this expected by looking at the equation (Eq. 3.31) but it is also expected due to the fact that the equation in principle is the same as the partial derivative for PPN-γ, which has been tested extensively (Hobbs et al., 2010). The only thing different in the two partial derivatives is that where the mass-derivative has $(1 + \gamma)$ the PPN-γ one instead has M_L (can be seen by looking at Eq. 3.8 for our model and Eq. A.8 for GREM) and this means that if it is shown to be possible to solve for masses using this method, even higher accuracy should be achievable using the already existing GREM framework for PPN-γ with slight modifications.

4.2 Realistic simulations - Exploring the mass-distance parameter space

4.2.1 Detectability

This test is done in the same way as described in Section 4.1, except that in this case both attitude noise and source noise was turned on. The detection criterion used is; if the three most nearby sources to the lens had a Gaussian GoF with a $\sigma \geq 3$, it is counted as a detection; the selection of and motivation for this criterion is discussed extensively in section 4.3.1. The simulation was repeated whilst the lens kept being moved farther away, until the detection criterion was no longer met. This was done for bodies of different masses, for three different background source densities and at three different inclinations relative to the ecliptic (these inclinations correspond to the declination, δ since $y = 0$ in the BCRS in the test cases). This was done for a few reasons such as: the size of the parallax motion depending on δ, the number of measurements at different positions on the sky varying and the source density being drastically different in different regions of the sky. The table below shows the different simulations:

Source density	Declinations		
2000 deg^{-2}	$\delta = 0°$	$\delta = 45°$	$\delta = 90°$
10000 deg^{-2}	$\delta = 0°$	$\delta = 45°$	$\delta = 90°$
30000 deg^{-2}	$\delta = 0°$	$\delta = 45°$	$\delta = 90°$

Table 4.1: The table shows the different simulations done, they were done in three different sets grouped according to their source densities and will be referred to as set 1, 2 and 3 with set 1 being the lowest source density. Figure 4.22 shows where each of the simulations are valid.

For each set the simulation was done for seven different relevant masses for bodies described in Section 2.4.

Mass	Maximum distance		
	0°	45°	90°
1 M_j	400 AU	740 AU	780 AU
10 M_j	1850 AU	3 300 AU	3 900 AU
80 M_j	4 700 AU	9 300 AU	12 000 AU
1 $M_\odot$	19 000 AU	34 000 AU	40 000 AU
20 $M_\odot$	0.4 pc	0.68 pc	0.82 pc
1 000$M_\odot$	2.6 pc	3.1 pc	4.0 pc
10 000$M_\odot$	12.1 pc	19.9 pc	20.4 pc

Table 4.2: The results from the first set of simulations. The table shows the range at which the criterion for detection is no longer met.

The figure below shows the data plotted

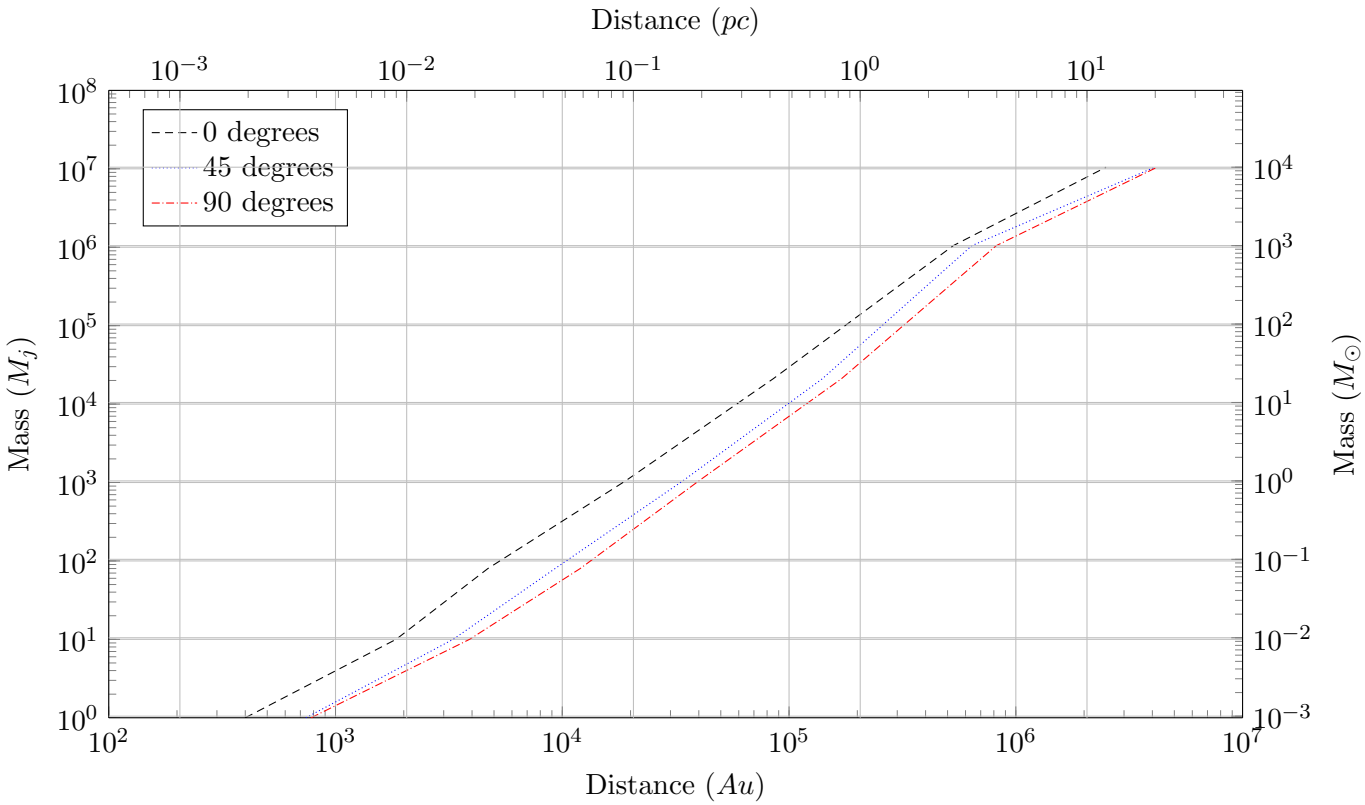

Figure 4.15: The results from the first set of simulations, done with a source density of 2000 deg^{-2}. Fitting straight lines to each of the curves we get the following:
Black: M = 1.91d − 11.7
Blue: M = 1.97d − 13.4
Red: M = 1.97d − 13.7

The simulations were then repeated with a higher source density.

Mass	Maximum distance		
	0°	45°	90°
1 M_j	1 000 AU	1 500 AU	1 500 AU
10 M_j	3 600 AU	6 400 AU	7 200 AU
80 M_j	11300 AU	16 200 AU	18 000 AU
1 $M_\odot$	40 000 AU	70 000 AU	70 000 AU
20 $M_\odot$	0.82 pc	1.1 pc	1.2 pc
1 000$M_\odot$	4.4 pc	8.2 pc	9.7 pc
10 000$M_\odot$	72.7	121.2 pc	169.7 pc

Table 4.3: The results from the second set of simulations. The table shows the range at which the criterion for detection is no longer met.

Plotting the data we get

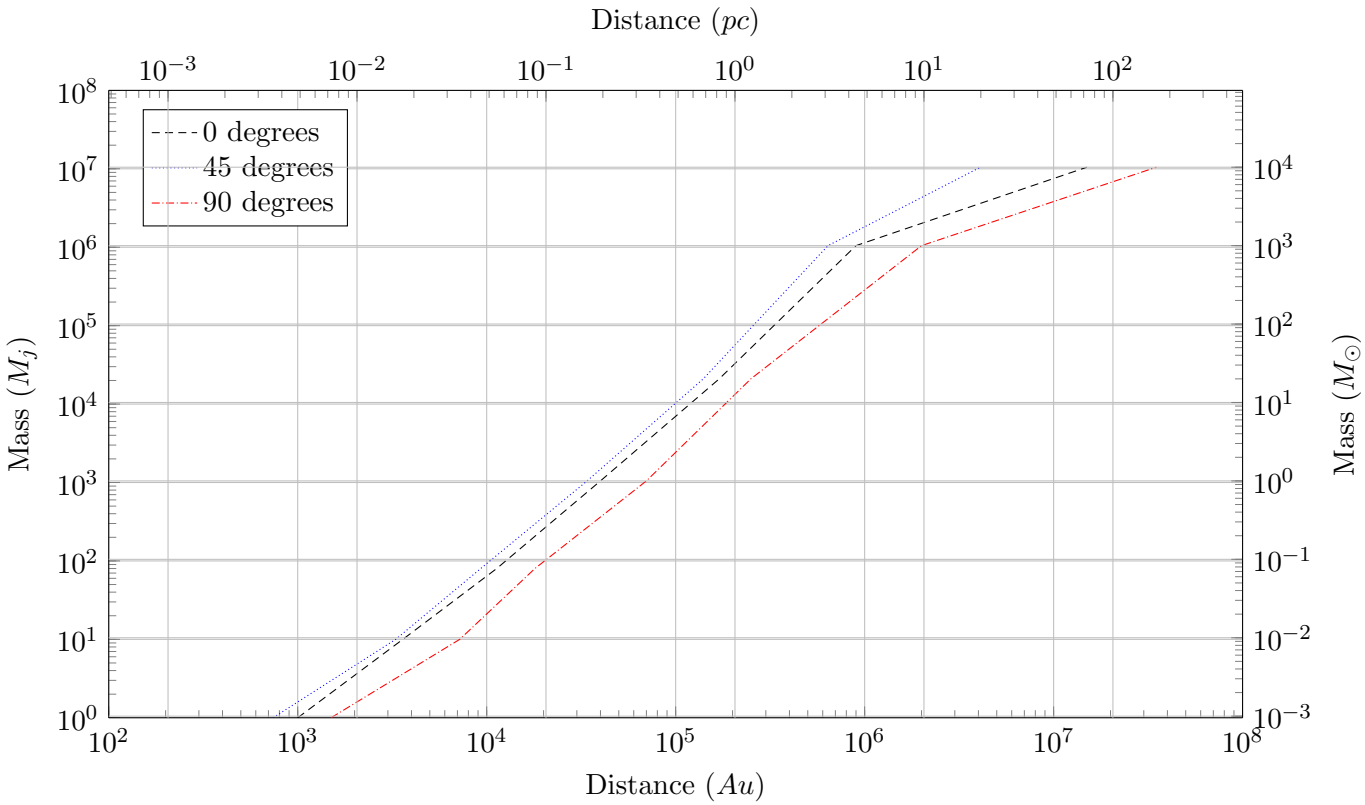

Figure 4.16: Results from second set of simulations, done at a source density of 10000 $\deg^{-2}$. Fitting straight lines to each of the curves we get the following:
Black: M = 1.78d − 12.0
Blue: M = 1.76d − 12.6
Red: M = 1.71d − 12.3

Then the simulations were repeated once again for the highest source density.

Mass	Maximum distance		
	0°	45°	90°
1 M_j	1 400 AU	1 700 AU	1 800 AU
10 M_j	4 600 AU	9 600 AU	11 500 AU
80 M_j	24 000 AU	47 000 AU	55 000 AU
1 $M_\odot$	0.6 pc	1.1 pc	1.3 pc
20 $M_\odot$	2.2 pc	4.6 pc	4.9 pc
1 000$M_\odot$	21.8 pc	43.6 pc	48.5 pc
10 000$M_\odot$	266.6 pc	727.2 pc	969.6 pc

Table 4.4: The results from the third set of simulations. The table shows the range at which the criterion for detection is no longer met.

The figure below shows the data from the table below plotted

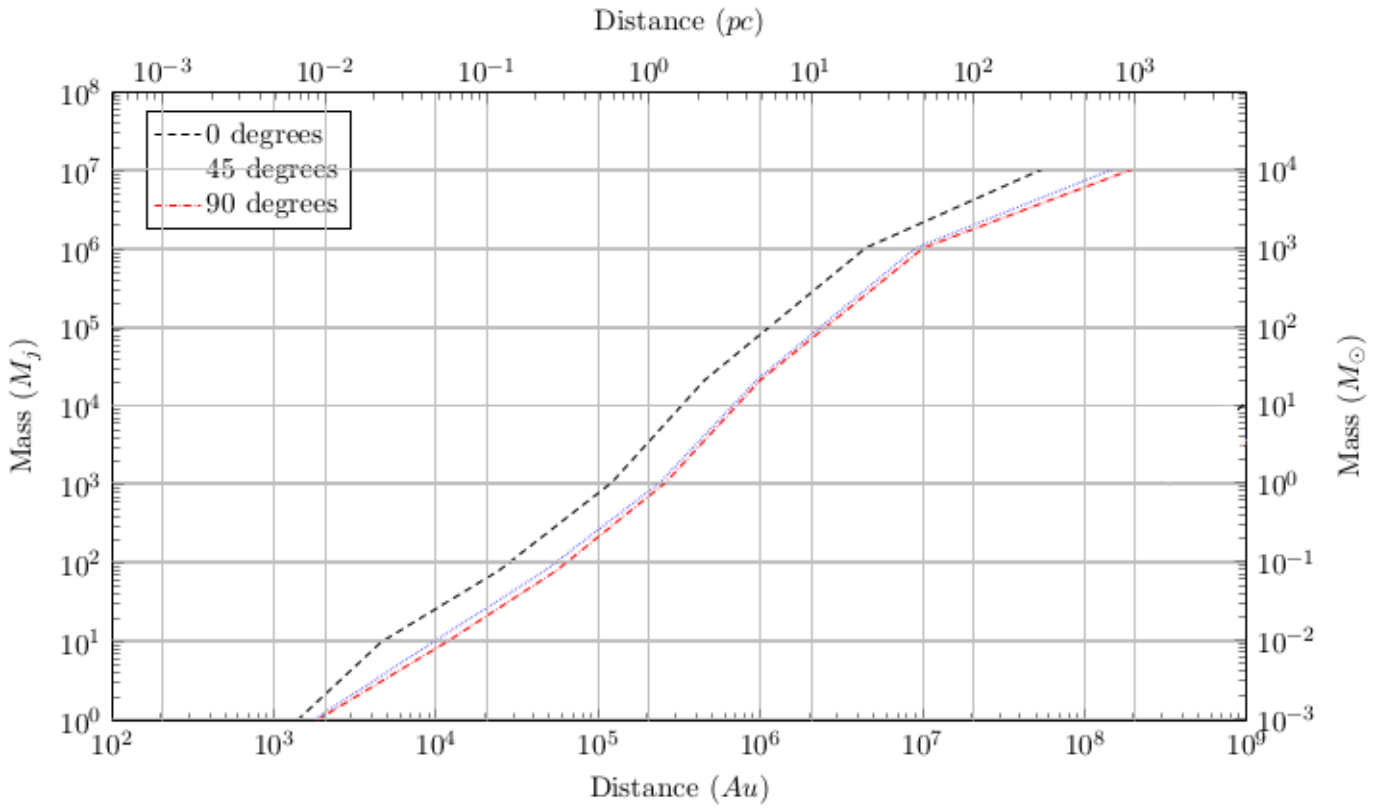

Figure 4.17: Results from second set of simulations, done at a source density of 30000 $\deg^{-2}$. Fitting straight lines to each of the curves we get the following:
Black: M = 1.58d − 11.2
Blue: M = 1.51d − 11.3
Red: M = 1.49d − 11.3

It is apparent the estimation made in in section 3.1 was far too optimistic. How the detection criterion affected it is discussed in Section 4.3.1 but it is not the only thing that affects it, other factors which were ignored in the initial estimation are also important. In the estimation, the parallax motion of the lens was ignored and it is important because it is what enables us to make a detection. The fact that the lens has a different parallax than the source it lenses means that the source will appear in a

different position, depending on when it is observed. This is what gives rise to the bad fits which are seen in the Gaussian GoF, if the lens and source did not have a different parallax motion it would mean that the source always would appear in the same 'wrong' place. In that case the source will always be lensed in the same way and we would not be able to tell the difference. The fact that the area covered by the parallax motion scales as $1/d^2$ could help explain why the curve does not have a slope of 1.

There is also the fact that the mass-distance relation is shifted to lower values. This can be explained by considering that it was estimated at what distance a single deflection would be detected. But in order to have a significant effect on the Gaussian GoF there has to be a lot of lensing events measured for each source. Requiring more deflections per source in the estimation would yield a similar result in shifting the relation. With these relations we can calculate the number of expected detections of different bodies. This calculation is done in Section 4.3.1.

4.2.2 Mass determination

For the determination of masses the same sets of simulations were done as shown in Table 4.1. The same masses were also tested for in each set except that the lowest mass tested was that of Neptune (≈ 0.054 M$_j$). The difference from the previous simulation is that here the algorithm is trying to solve for the mass. The simulations were set up such that the initial guess on the mass differed from the true mass by 50%. How good convergence the simulation gives will depend on the strength of the lensing, so two different results are presented in this section; the limits at which you get 1% and 10% accuracy. The accuracy for each run is given by looking at two different things, the *formal error* which is given by taking the square root of the diagonal element from the inverse matrix corresponding to the mass-derivative in Eq. B.6 in Appendix B. The formal error is given directly from the solution and is a measure of how well-determined the solution is. It was then compared to the *true error* which is simply the true value minus the running value, this will of course never be known in the real mission. Table 4.5 shows the result from the first set of simulations.

Mass	Maximum distance		
	0°	45°	90°
Neptune	270 AU	350 AU	350 AU
1 M_j	1 800 AU	2 200 AU	2 400 AU
10 M_j	∼10 000 AU	∼10 000 AU	∼10 000 AU
80 M_j	∼10 000 AU	∼10 000 AU	∼10 000 AU
1 $M_\odot$	∼10 000 AU	∼10 000 AU	∼10 000 AU
20 $M_\odot$	∼10 000 AU	∼10 000 AU	∼10 000 AU
1 000$M_\odot$		Simulation unstable	
10 000$M_\odot$		Simulation unstable	

Table 4.6: This table shows the 10%-limit for the lowest source density, 2 000 deg^{-2}. For an explanation on the ∼10 000 AU and Transit error, see the caption of table 4.5.

The tables below show the results for the second set of simulations.

Mass	Maximum distance		
	0°	45°	90°
Neptune	170 AU	230 AU	230 AU
1 M_j	350 AU	430 AU	430 AU
10 M_j	1 300 AU	2 100 AU	2 500 AU
80 M_j	3 100 AU	5 500 AU	6 000 AU
1 $M_\odot$	∼10 000 AU	∼10 000 AU	∼10 000 AU
20 $M_\odot$	∼10 000 AU	∼10 000 AU	∼10 000 AU
1 000$M_\odot$		Simulation unstable	
10 000$M_\odot$		Simulation unstable	

Table 4.5: This table shows the 1%-limit for the lowest source density, 2 000 deg^{-2}. There are two things in this that will be immediately noticed, the first is the ∼10 000 AU. What that means is that the algorithm works just fine and we get 1% fits up until ∼10 000 AU but then the simulation will start to diverge on a regular basis. It does not mean that it is impossible to determine masses at greater distances though, what it means is that for most initial conditions the simulation will diverge. This is likely a purely numerical effect and comes from the way Eq. 3.31 is set up. This is discussed in detail in section 4.3.2. When it says that the simulation is unstable in the table it means that the simulation crashed due to it being unable to determine the transit. This means that the lens is so massive that it cannot be determined when sources cross the CCDs because they are being deflected too much in the region where it should be possible to get reliable determinations of their mass, i.e. at $d < 10000$ AU.

Mass	Maximum distance		
	0°	45°	90°
Neptune	330 AU	540 AU	540 AU
1 M_j	750 AU	1 100 AU	1 100 AU
10 M_j	∼10 000 AU	∼10 000 AU	∼10 000 AU
80 M_j	∼10 000 AU	∼10 000 AU	∼10 000 AU
1 $M_\odot$	∼10 000 AU	∼10 000 AU	∼10 000 AU
20 $M_\odot$	∼10 000 AU	∼10 000 AU	∼10 000 AU
1 000$M_\odot$		Simulation unstable	
10 000$M_\odot$		Simulation unstable	

Table 4.7: This table shows the 1%-limit for the middle source density, 10 000 deg^{-2}. For an explanation on the ∼10 000 AU and Transit error, see the caption of table 4.5.

Mass	Maximum distance		
	0°	45°	90°
Neptune	490 AU	690 AU	690 AU
1 M_j	4 100 AU	6 800 AU	6 900 AU
10 M_j	∼10 000 AU	∼10 000 AU	∼10 000 AU
80 M_j	∼10 000 AU	∼10 000 AU	∼10 000 AU
1 $M_\odot$	∼10 000 AU	∼10 000 AU	∼10 000 AU
20 $M_\odot$	∼10 000 AU	∼10 000 AU	∼10 000 AU
1 000$M_\odot$		Simulation unstable	
10 000$M_\odot$		Simulation unstable	

Table 4.8: This table shows the 10%-limit for the middle source density, 10 000 deg^{-2}. For an explanation on the ∼10 000 AU and Transit error, see the caption of table 4.5.

Mass	Maximum distance		
	0°	45°	90°
Neptune	400 AU	730 AU	730 AU
1 M_j	900 AU	1 400	1 400 AU
10 M_j	∼10 000 AU	∼10 000 AU	∼10 000 AU
80 M_j	∼10 000 AU	∼10 000 AU	∼10 000 AU
1 $M_\odot$	∼10 000 AU	∼10 000 AU	∼10 000 AU
20 $M_\odot$	∼10 000 AU	∼10 000 AU	∼10 000 AU
1 000$M_\odot$		Simulation unstable	
10 000$M_\odot$		Simulation unstable	

Table 4.9: This table shows the 1%-limit for the highest source density, 30 000 deg^{-2}. For an explanation on the ∼10 000 AU and Transit error, see the caption of table 4.5.

Mass	Maximum distance		
	0°	45°	90°
Neptune	600 AU	950 AU	950 AU
1 M_j	6 100 AU	∼10 000 AU	∼10 000 AU
10 M_j	∼10 000 AU	∼10 000 AU	∼10 000 AU
80 M_j	∼10 000 AU	∼10 000 AU	∼10 000 AU
1 $M_\odot$	∼10 000 AU	∼10 000 AU	∼10 000 AU
20 $M_\odot$	∼10 000 AU	∼10 000 AU	∼10 000 AU
1 000$M_\odot$		Simulation unstable	
10 000$M_\odot$		Simulation unstable	

Table 4.10: This table shows the 10%-limit for the highest source density, 30 000 deg^{-2}. For an explanation on the ∼10 000 AU and Transit error, see the caption of table 4.5.

From the simulations it has become apparent that there are two different ways in which the simulation becomes unstable and diverges. The first one, shown in Fig. 4.18 is as we expect the simulation to behave. The left panel shows a converging fit when the signal is very weak, in this case it is a Neptune located at 500 AU. The weakness of the signal is evidenced in the fact that it takes 150 iterations for the solution to converge. The right panel shows the same setup except that in this case the lens has

been moved to 1 000 AU and here the signal is too weak, which means that the algorithm will not be able to reach convergence and it does not.

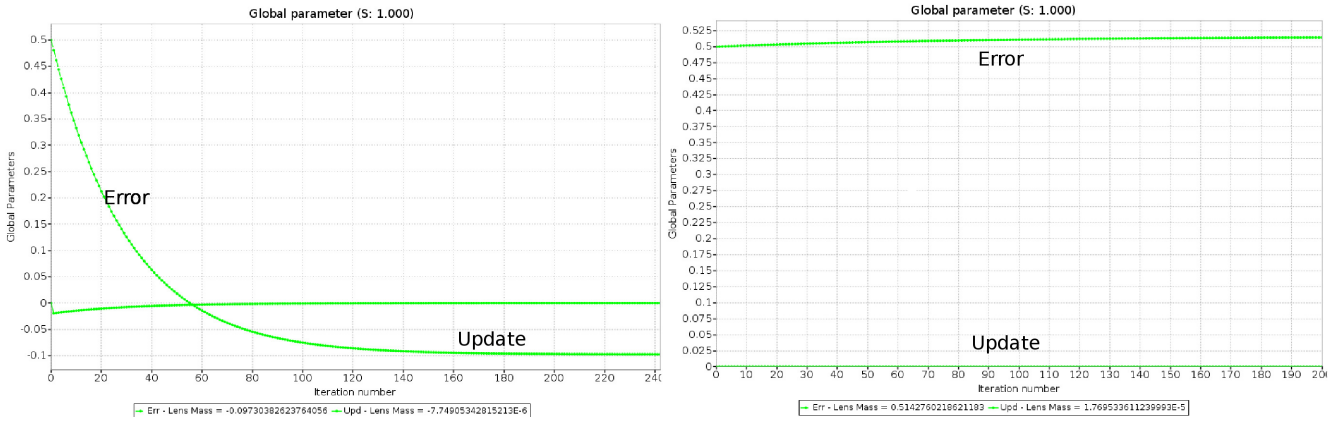

Figure 4.18: The left panel shows the convergence of the fit for a Neptune mass lens located at 500 AU. The lensing signal is weak, which means that the update will be small, so it takes a lot of iterations to reach convergence. The right panel shows an attempted fit to a Neptune mass lens located at 1 000 AU. At that distance the signal from the lens is too weak to be solved for, which is shown by the fact that the update is close to zero. There is a small update, which goes in the wrong direction indicating that it is dominated by numerical noise.

Why this happens can be seen in the Gaussian GoF in the Fig. 4.19. The left hand panel shows the 500 AU, converging run. Whereas the right hand panel shows the diverging run.

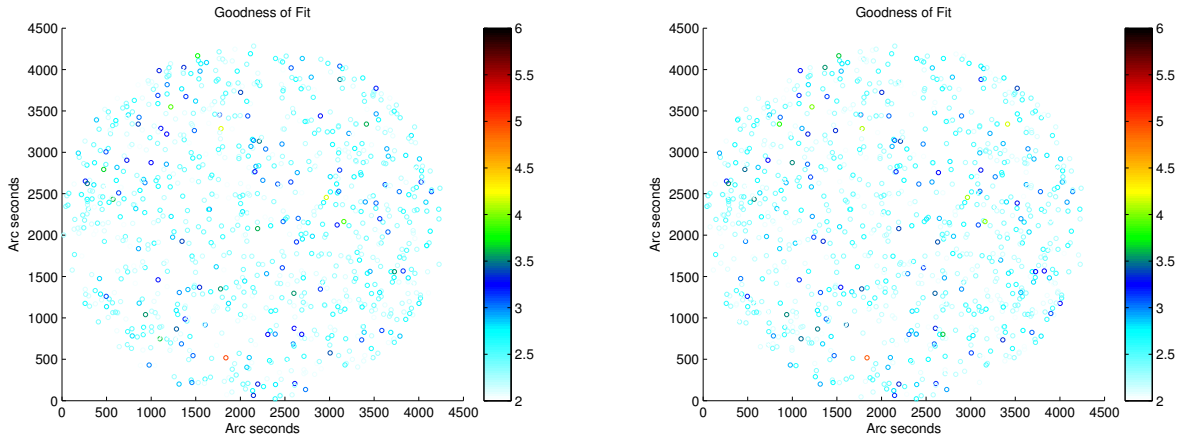

Figure 4.19: The left panel shows the Gaussian GoF of the stars being perturbed by the Neptune mass body at 500 AU in the run that converged. The right panel shows the diverging run with a Neptune mass lens at 1 000 AU. The plot only shows sources with $\sigma > 2$ and it is hard to make out just by looking at it, but if one looks carefully at the center of both plots it can be seen that there are slightly more sources that are more perturbed in the left panel than in the right. This is sufficient to achieve convergence.

Figure 4.20 shows the second type of divergence. For this particular set of initial conditions the divergence occurs at 11 500 AU. The left panel shows a converging run and the right panel shows the

exact same setup except that lens has been moved out to 11 500 AU, this is only an increase by 4.5%. Yet it results in a rapidly diverging run, because the divergence in the end is as large as it is; it cannot be resolved in the figure that it starts diverging from the first iteration. But it does.

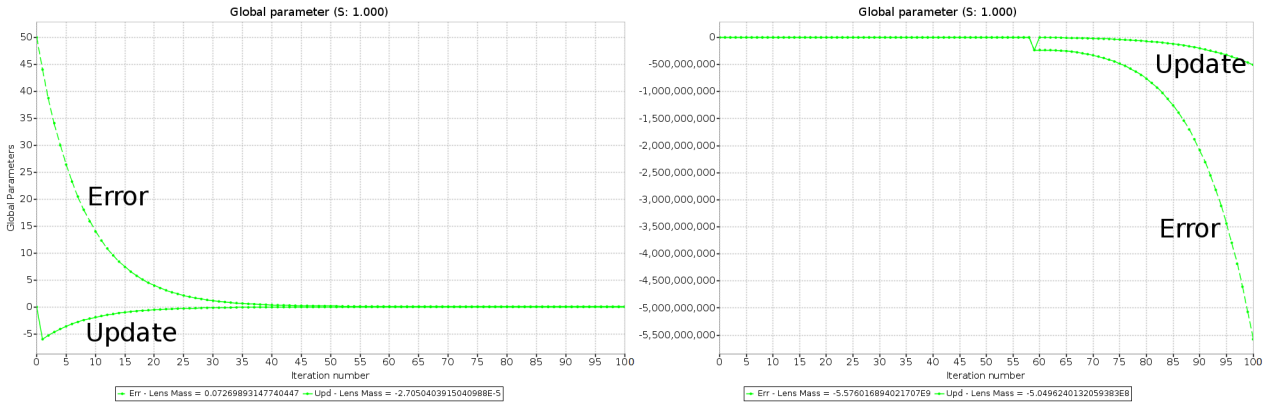

Figure 4.20: The left panel shows a converging run when solving for a 100 M_j lens at a distance of 11 000 AU, The right panel shows the same simulation but the lens moved to 11 500 AU, in the second case it rapidly diverges.

This can be further exemplified by looking at the Gaussian GoF of the two runs. Figure 4.21 shows the converging 11 000 AU run on the left side and the diverging 11 500 AU run in the right panel.

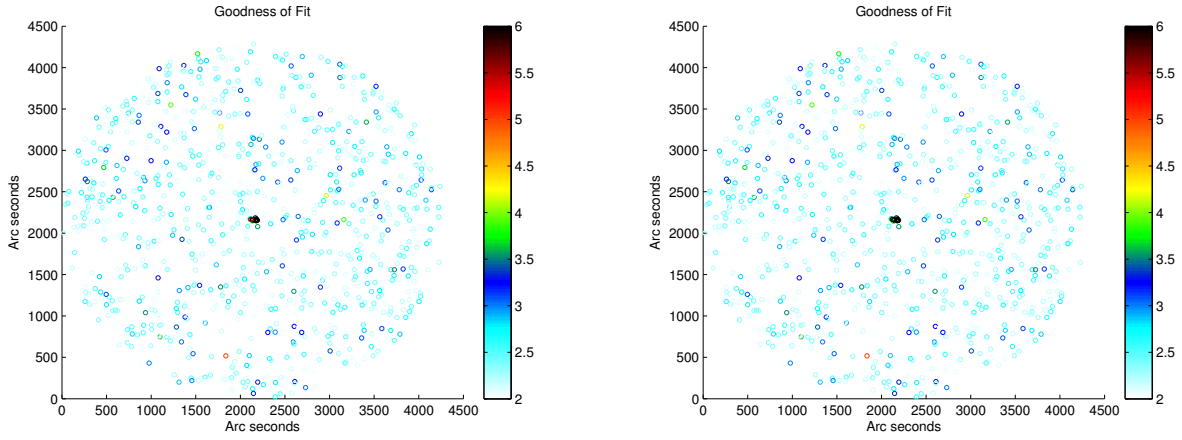

Figure 4.21: Unlike Fig. 4.19 which shows that the simulation diverges because the signal from the lens becomes too weak this figure shows the other kind of divergence. The left panel shows the converging run whereas the right panel shows the diverging run. The only thing different between the two runs is that the lens in the left panel is located at 11 000 AU whereas the one on the right side is located at 11 500 AU. The signal from the lens is very strong in both cases and the simulation still diverges as explained in the text.

4.3 Conclusions & Discussion

4.3.1 Detectability

The patterns discussed and shown (Figs. 4.6, 4.7, 4.8) will almost never actually appear in the goodness of fits. This is because the source density is simply too low. The three different densities give an average angular separation of 45.4, 20.3 and 11.7 arcseconds. For the pattern to be seen the lens must cross several sources. Let us assume that for the pattern to be seen the lens parallax must be $\gtrsim 100$ as, this would mean that the patterns only would appear for bodies within 2000 AU. Considering what was shown in Fig. 4.10 and discussed in at the end of this section ("Detecting Solar system objects") we know that bodies that are too near become nearly undetectable by looking at the Gaussian GoF. This means that in no part of the mass-distance parameter space will there be a body that would be hitherto undetected which would give rise to the patterns.

So, why use the Gaussian GoF as a detection criterion? The primary reason for it is that it is a readily available statistic for every source in the vast Gaia catalog. It has not yet been mentioned, but finding a signal from a lens in the Gaia catalog will not be a trivial task, which makes using something as straight forward as the Gaussian GoF desirable. Another thing to be mentioned regarding the criterion is that we use three stars with bad fits. Why three? Looking at single stars, there will be bad fits on stars. These bad fits could be due to a variety of reasons, including having a planetary system, being a wide binary or the star having some sort of variability. If we were to look at two stars there will also be a lot of bad fits, in fact there might be even more double bad fits than there are singles. This because a large fraction of stars are in binary systems which will cause the fit to be bad. Finding three adjacent stars with bad fits would be highly unlikely barring there being something, such as a cloud of gas obscuring that particular line of sight or they could of course be in a triple star system. These systems are far less common than the binaries and it would warrant further study either way. Another reason for having three perturbed sources is the degeneracy of the lensing equation that was mentioned previously. Having at least three sources that are highly perturbed will make fitting a lensing model to the observation more likely as compared to having only one or two sources. Combining these two criterion makes for a strict definition of detection and with this criterion in place we find the following relations:

For $\rho = 2000\text{deg}^{-2}$ at 0°, 45° and 90° above the ecliptic

$$\begin{aligned} M &= 8.29 \times 10^{-6} d^{1.91} \\ M &= 1.67 \times 10^{-6} d^{1.97} \\ M &= 1.12 \times 10^{-6} d^{1.97} \end{aligned} \tag{4.4}$$

For $\rho = 10000\text{deg}^{-2}$ at 0°, 45° and 90° above the ecliptic

$$\begin{aligned} M &= 6.14 \times 10^{-6} d^{1.78} \\ M &= 3.37 \times 10^{-6} d^{1.76} \\ M &= 4.55 \times 10^{-6} d^{1.71} \end{aligned} \tag{4.5}$$

For $\rho = 30000\text{deg}^{-2}$ at 0°, 45° and 90° above the ecliptic

$$\begin{aligned} M &= 1.37 \times 10^{-5} d^{1.58} \\ M &= 1.27 \times 10^{-5} d^{1.51} \\ M &= 1.27 \times 10^{-5} d^{1.49} \end{aligned} \tag{4.6}$$

The reason for testing at three δ is two fold. Firstly, the area covered by the lens' parallax motion will increase with an increasing δ. Secondly, if we look at Fig. 1.4 which depicts the scanning law

of Gaia we see that the number of measurements vary by up to a factor of five with position on the sky. The least amount of measurements will be done in the ecliptic and there is an over-density of measurements at 45° which makes the number of measurements there roughly double that of the number of measurements that will be done at 90°. From the results we can see that there is almost no difference between the tests done at 45° and 90° even though the projected area that the lens sweeps across differs by a factor of two and since the number of scans between the two positions also differ by a factor of two; we can conclude that the area covered by the parallax motion and the number of scans scales our detection equally. Looking at the difference between 45/90° and 0° we see that larger number of measurements and larger area covered done appear to improve the scaling. The differences are however on the same level as the uncertainty in these tests.

With the scaling relations we can now do some predictions on the number of detections. Here follows a prediction for the number of detections of various kinds of bodies, based on the approximations made in sections 2.4-2.6 and the scaling relations given in this section. The first thing to do is to see which of the relations should be used where. Figure 4.22 shows the same thing as Fig. 1.4 except that the region which is valid for each density and δ is highlighted.

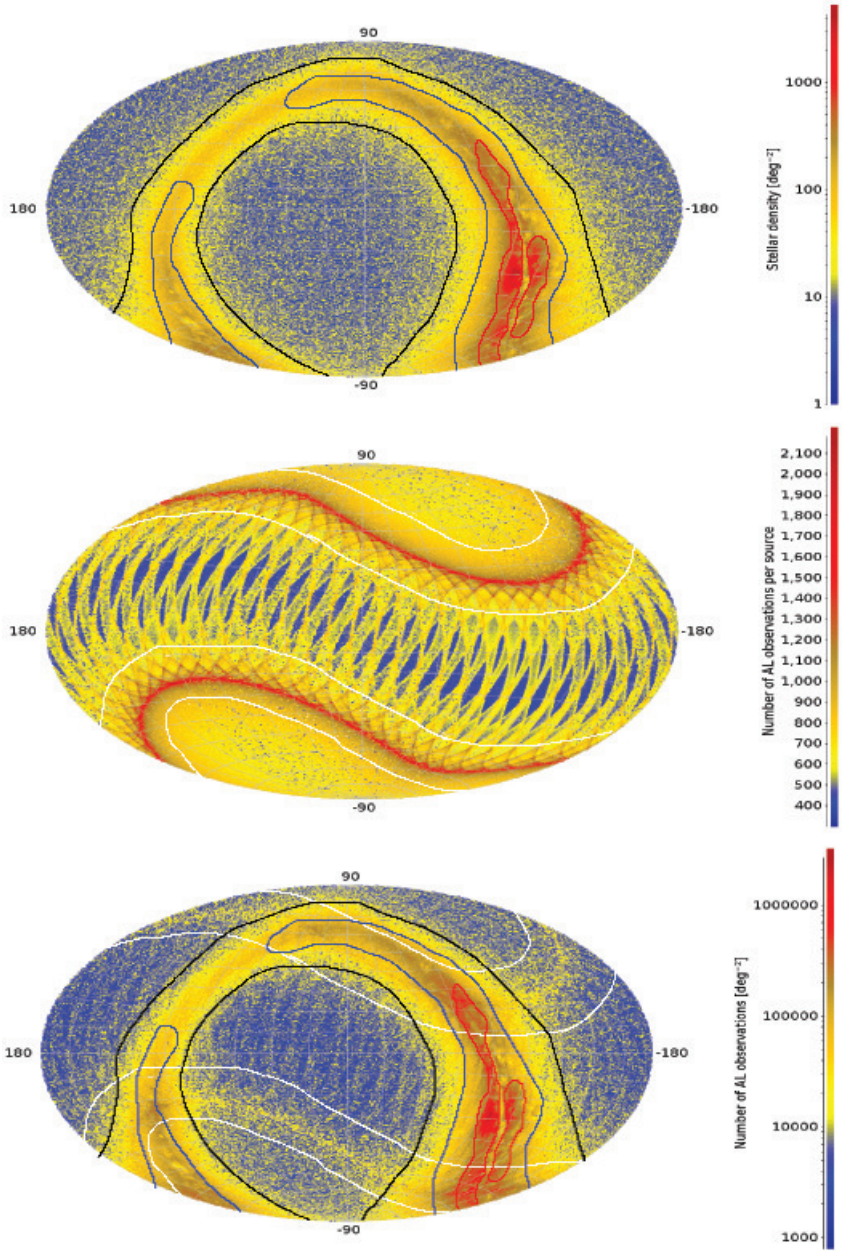

Figure 4.22: This figure shows the same thing as Fig. 1.4 and just like in that one it should be noted that the skymaps come from a simulation with 2×10^6 sources, to match our assumption we scale up the density by a factor of 50. Unlike Fig. 1.4 in this figure the the three different densities tested have been highlighted in the top panel. They are as follows: Red ≥ 30000 deg^{-2},Blue $= 10000-30000$ deg^{-2} and **Black= 2000 − 10000 deg^{-2}**. The middle panel shows the zones in which the three different inclinations tested will be used. in the calculation, there are areas in each zone where there will be more scans and areas where there will be less. Considering the fact that was discussed on the previous page, i.e. that the area covered by the parallax motion scales the same way as the number of measurements. The average of covered area by the parallax and number of scans on that area will be roughly the same in each region and thus the scaling will be roughly the same. The bottom panel shows the two outlines overlaid on each other. There will be a large fraction of the sky that is not included in the calculation as the source density was too low to be tested.

	2000 deg^{-2}	10000 deg^{-2}	30000 deg^{-2}
0°	8%	2.5%	1.5%
45°	6.5%	5.5%	1%
90°	5.5%	1.5%	-

Table 4.11: The fraction of sky covered by each of the derived relations.

The last thing needed to calculate the number of detections is the mass distribution of a given body. Then the detection rate can be given by:

$$n = \sum_{i=1}^{9} f_i \int_{M_{min}}^{M_{max}} \left(\frac{d_i}{R}\right)^3 \left(\frac{dN}{dm}\right) dm \tag{4.7}$$

where n is the number of expected detections, the sum is over each region as shown in the bottom panel of Fig. 4.22, f_i is the fraction of the sky that each region covers. The integral goes from the minimum and maximum mass the given body can have, d_i comes from the relations shown before, the R is from Eq. 2.13 which means that the fraction of the two cubed gives the number of 'unit volumes' a body of a given mass fills. The second fraction is the mass function of the selected body.

The mass function used to calculate the different rates are:

- **Black Holes**
  The mass function used is given by Özel et al. (2010). The mass distribution is stated to be well represented by a Gaussian distribution with $\mu = 7.8M_\odot$ and $\sigma = 1.2M_\odot$. Putting in the numbers we get that the expected number of detections to be $1-6\times10^{-5}$ depending on the value of R used.

- **Neutron Stars**
  The mass function used here is given by Kiziltan et al. (2013). The study shows that there are two distinct mass distribution, depending on the companion of the neutron star as they are mostly found in binaries. Two different distributions are presented, one for double neutron star systems and one for neutron star - white dwarf systems. For the calculation the neutron star - white dwarf mass distribution of neutron stars will be used as they are far more prevalent in the Galaxy. The mass distribution is well modeled as a Gaussian distribution with $\mu = 1.55M_\odot$ and $\sigma = 1.35M_\odot$. Putting the numbers in we get a value of $2 - 5 \times 10^{-5}$.

- **Brown Dwarfs**
  The mass function used for the calculation here is the same as the one that was used to calculate the number of brown dwarfs in the Galaxy, i.e. the Kroupa (2001) IMF. The reason we can use the IMF here and not for the heavier bodies is simple, their progenitors undergo stellar evolution whereas the brown dwarfs are the progenitors themselves. Brown dwarfs do not undergo any stellar evolution, thus their mass function should be identical to their IMF. The distribution given is $dN/dm \propto m^\alpha$ where $\alpha = 0.3 \pm 0.7$. Doing this, we get the expected number of detections to be $1-3\times10^{-5}$. Seeing as how the R calculated in section 2.4.3 probably was significantly larger than what it is in reality because of the assumed distribution of brown dwarfs the number of detections should probably be even lower.

We have to point out that the simplistic approximation for R in sections 2.4 are quite pessimistic. Taking the black holes as an example, more detailed studies such as Fender et al. (2013) or Maccarone (2005) which give the most conservative estimates of R gives a value of 7.6 pc. Redoing the calculation for black holes we instead see that there instead will be $\sim 4\times10^{-4}$ detections. Assuming neutron stars

follow the same distribution but there just being more of them, we get that there will be $0.001 - 0.003$ detections of neutron stars.

We now have to consider the fact that the mass-distance relation that was predicted in Section 3.1 and what was tested are not the same thing. The prediction shows at what distance a single lensing event from a given body should be detectable whereas what we tested shows the probability of detecting a given body. Detecting a *lensing event* and detecting a *lens* are two different things as the latter should allow for a lensing model to be fit to the observation. This means that the predictions made from studies such as Belokurov & Evans (2002), which put the number of predicted lensing events in the thousands, do not contradict our findings. But finding a single lensing event amongst the Gaia data will be a difficult thing, besides the pure size of the catalog is also the fact that there will be many outlier measurements even without lensing. Then there is also the question of how much information can be gotten from finding a single lensing event.

The aim of this test was to investigate whether there existed a comparatively simple, reliable and statistically significant method of searching for lenses in the Gaia data. From the results and predicted detections it is evident that looking for lenses with the method tested in is unlikely to yield positive results. It does not mean that Gaia will not be able to detect lenses, it does not even mean that using the Gaussian GoF of the sources is the wrong way of looking for lenses. The simulations consistently showed that what would happen as the lens was moved farther out was that the nearest of the three sources to the lens would remain highly perturbed ($\sigma \gtrsim 6$) as the Gaussian GoF of the adjacent two would go under 3 σ causing the criterion no longer to be met. If one kept moving the lens farther out the central source would generally remain highly perturbed at much farther distances. Frequently up to ten times farther and even more in some cases. Knowing this, one can estimate the number of detections for only using a single highly perturbed source as detection criterion by just scaling up the distance at which a given body can be found by a factor of 10 (this is a rough approximation so we just scale it up linearly, in reality changing the criterion would probably affect the exponent as well, bringing it closer to 1). Redoing the calculations we now find that we can expect to detect ~ 0.4 black holes, $1 - 3$ neutron stars and $0.01 - 0.03$ brown dwarfs.

Now, purely from a statistical point of view ~ 400 out of 10^8 sources will have $\sigma \gtrsim 6$. These will all be investigated in some way and a variety of different models will be attempted to be fit to them such as planetary orbits or wide binaries. If no other model fits it is likely that the bad fit could be due to the presence of a lens since 1% of these bad fits could be due to lenses. In that case one would have to try to reduce the residuals by applying a lensing model, not the one presented in this work as it has been shown to be unstable due to the non-linear effects. The fact that it is only one highly perturbed source makes it even harder. Some other model would have to be developed for this, likely using the 2D lensing equations along the lines of what was proposed in Belokurov & Evans (2002) which is discussed in Section 4.3.3. What this shows however is that a significant fraction of sources with large Gaussian GoF values could be the result of lensing.

The number of detections is equally sensitive to the value of d. As an example, the value of d given by Fig. 3.1 larger by a factor of $10^3 - 10^4$ for Solar mass bodies. As it has been discussed we know that the estimation made there is not representative of reality but we also know that lensing events can be detected at those distances. This suggests that there should be a better statistic to use in the search for lenses than the Gaussian GoF. One potential statistic to look at is the variability of α and δ measurements for specific sources. Exactly how this would be done is not self-evident, the point is however that this kind of variability will be measured for many sources which will not be considered to be bad fits by looking at their Gaussian GoF.

Detecting Solar System Objects

The reason that masses lower than a Jupiter mass were not tested for is the large parallax motion such a body would have at a distance where its Einstein radius is sufficiently large for it to induce large deflections. This seems counterintuitive at first, yet it is actually quite simple. The large parallax motion will mean that more stars are lensed, which one might think is good but in this case it is not. What happens is that the deflections become diluted amongst more sources since the lens wont be near the same sources when the area is revisited and the source update will treat the lensed measurement as an outlier. Those measurements will be weighted when calculating the Gaussian GoF which means that if a source only has one or a few such outlying measurements it will show up as a 'good' source in the reduced data. If the aim is to find nearby massive bodies then instead of looking at the Gaussian GoF of the stars in particular regions, one could look for regions of the sky where there are more outliers in α and δ measurements than the average (or a region in which the outliers are unusually large), yet not enough for there to be a significant change in their GoF. In this region, if an ellipse could be traced in the outliers, it would indicate a body lensing these sources. Also, because of the large ellipse being traced one could look for effect shown in Fig. 4.24, this effect however is not sufficiently studied.

Detecting intermediate mass black holes

Drawing conclusions regarding these are nigh impossible even if they are assumed to exist. The predictions of the amount of them that exist in the Galaxy put the count to be low, as one would expect. But besides that they are also thought to have Halo-like orbits, making it hard to predict how many of them and how they would be distributed in the Disk; as it is the only place in which the stellar density is sufficiently high for them to be detected at large distances. Also, validity of the geometric model we use for light deflection becomes questionable for such high masses which could explain the behavior seen in Figs. 4.15, 4.16, 4.17 for high masses at large distances. The behavior that the curve starts flattening out, scaling better for some reason. This could also be due to the fact that at those distances the parallax motion of the lens will be much smaller than the distance between the sources meaning that the scaling could be much more similar to what is predicted in Fig. 3.1.

4.3.2 Mass determinations

The simulations show no clear systematic behavior when it comes to the determination of masses at least not in the same manner as when looking at the detectability. In fact, one can get very different results by just changing the random seeds which determine things such as source distribution. The method for determining masses used in this work has three potential uses:

- There is mounting evidence for the existence of a large body in the inner outer Solar system. This is the one region in which the mass determination works reasonably well. If such a body ever is discovered one could potentially determine its mass in a similar manner as shown here. The nice thing is that this will be possible to do even if the body is discovered long after Gaia has finished its mission since the information will be stored in the residuals.

- The mass of the Solar system ice giants is already well known. However, if this method of mass determination was implemented using GREM one could possibly determine the mass even better. Which in turn could lead to more science or it could just be the novelty of slightly improving upon the current mass estimation.

- The possibility of determining the masses of the nearby, large asteroids still exists as it has not been sufficiently explored. For the Kuiper belt objects it will however be impossible to determine

the mass in this manner. If it is possible to determine the mass of the nearby asteroids, it is because of the fact that their parallax motion will be large and they will cross a lot of sources. This is something that should be investigated more.

The reason for the exhibited divergent behavior is twofold. Firstly, the partial mass derivative given in Eq. 3.31 is independent of mass. This means that for the sake of the fitting it does not matter whether it is a Jupiter mass being solved for or 10^4 Solar masses. Secondly, the derivative scales as $1/r$ which means that the derivative becomes smaller the farther away the lens is placed. This means that for a given stellar background, the type of critical distance described in the previous paragraph will always appear no matter how massive the lens is and how strong the signal is. To understand why this happens we need to look at the least squares method described in Appendix B. It shows the basic principle behind solving a linear system of equations, i.e. the inversion of the matrix A. In the global block this A matrix consists of the partial derivatives of $\hat{\mathbf{u}}$ with respect to the global parameters, transformed using the field angle calculator to the appropriate astrometric derivatives. As the lens is moved farther away, these derivatives will start approaching zero (numerical noise) and when they do the update will diverge, because it is calculated from the inverse of the A matrix (Eq. B.6).

A method for determining masses of brown dwarfs was proposed by Smart (2012) in a Gaia technical note. Instead of incorporating the lens mass-solution into AGIS, the proposal was to monitor brown dwarfs as they move across the sky and as they approach stars use Gaia to see how much the star deviates from its track (Fig. 1.2). There are however two problems with this proposal that makes it practically unfeasible to do.

- The assumed astrometric precision is that of the background star, not of the brown dwarf. The two will be equally important and the maximum achievable precision for the brown dwarfs will be a lot lower than that of the brighter stars.
- The duration of each lensing event (and thus the number of measurements) has been overestimated. All the detected brown dwarfs are within a sphere of ∼100 pc, with most of them being around ∼30 pc. Most stars will be much farther away than that, which means that the parallax motion of the brown dwarf will be much greater and the close encounter will not last as long as the author suggests.

However, just because this method is not applicable for brown dwarfs does not mean that it is useless. As discussed previously the direct determination of stellar masses is quite important for astrophysics and also impossible with the method tested in this work. This method offers a way of doing things that could be better than doing it in the direct solution. Figure 4.23 shows a so called optical binary, the probability of having such a configuration can easily be calculated. Each 'good' star will occupy an area of:

$$\frac{41253}{10^8} \times 3600^2 = 5346 \text{ as}^2 \tag{4.8}$$

And the area occupied by two stars will simply be twice that. Now, for this to work we assume that the stars have to be within 0.1 as of each other. The probability of that occurring is given by:

$$\frac{0.1^2\pi}{10692} = 2.94 \times 10^{-6} \tag{4.9}$$

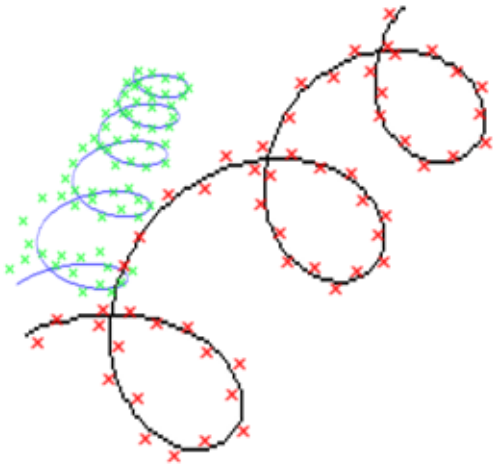

Figure 4.23: The figure shows an optical binary. The black line represents the motion of the foreground star and the blue line represents a background star. The red and green crosses are individual measurements done by Gaia. Each loop represents a years time, which means that the measurements on each of the loops are done at the same time. The figure shows that at the time during which they are close together the background star will be offset from its optimal fit. This offset could be used to directly determine the mass of the foreground star.

Considering there are 10^8 of these stars means that there will be ∼294 of these optical binaries observed by Gaia. Fig. 4.23 shows a case with one of these optical binaries where the proper and parallax motion will bring them closer and farther apart at different points in time. The advantage here is that because of the way Gaia works it will always measure the two stars at the same time. As an example, let us assume the foreground star to be a $1M_\odot$ star located at 100 parsec with a distant background star it will have an Einstein radius of ~ 9 mas. Them being within 0.1 as of each other will result in the deflections being $\gtrsim 0.8$ mas. In a case such as this several measurements will have been made of the background star, in some cases the effect from the lens will be lower than the precision in the measurement whereas in a some other cases the lensing will be noticeable. The measurements in which the lensing is noticeable will be considered outliers and will be weighted to not affect the fit of the stellar parameters as much. This means that by finding a relation for the deviation from the fit as a function of angular separation between the two sources will be a direct measure of the mass of the foreground star.

This way of determining masses was not tested as part of this work and requires testing to see if it works better or worse than solving for the mass as part of the full solution.

4.3.3 Fitting the lensing model

The problems regarding fitting the 3D lensing model to the observation was discussed in detail in section 4.1 in regards to the initial simulations. It was shown to require very precise initial guesses to be able to reach convergence, which makes it unreasonable do the fit for bodies detected in the residuals; it could however be used for visible bodies. If there is a visible body whose mass is not well determined and position known to a somewhat high precision. One could attempt to determine the mass to as high a precision as possible given the uncertainty. Then, given the fact that the position is already well known one could attempt to determine it improving upon the old value. This will allow

for an even better determination of the mass and if this process is carefully repeated one could end up with a better determination of the mass than by just fitting the mass. Or rather than doing it this way one could implement an algorithm that is better at dealing with non-linear problems, how well either would work is not yet known.

It could be possible to get around the non-linearity of the problem all together. Belokurov & Evans (2002) put forward a way of fitting a lens to an observation in a nearly linear fashion in the same manner as solving for the astrometric parameters. The problem is however that this method utilizes the so called proper motion angle (as defined in Gould & Salim, 1999). This method of solving for lenses with Gaia was derived at a time when Gaia still was supposed to have an interferometer and the SIM mission was supposed to compliment the measurements. But SIM never happened and Gaia never got the interferometer making this way of doing things impossible. But something similar could be developed.

4.3.4 Additional comments

Using a stationary lens

The only case where having a lens in motion would make things worse is when a fit to the observation is attempted, as it would introduce even more complexity to the problem. Even in that case, the motion of the lens is simply the time derivative of the position which is being determined and with a 5+ year baseline, including it might not be that problematic. For the sake of detectability, it could on the other hand make things better because as discussed in the previous section it is the differences in angular separation between lens and source that gives rise to the bad fits that we use as detection criterion. For a lens in motion the differences will almost always be greater and also more sources would be perturbed and this might improve the detectability. As for the patterns shown in Figs. 4.7, 4.6 and 4.8, these patterns would be broadened by having a moving lens. We have however showed that these patterns will not be seen in Gaia data so this can be ignored. When it comes to determining masses we assume the position of the lens to be known which would mean that we also assume the motion to be known.

Zero-parallax objects

The observed effect is easily understandable and explained is explained in the figure below.

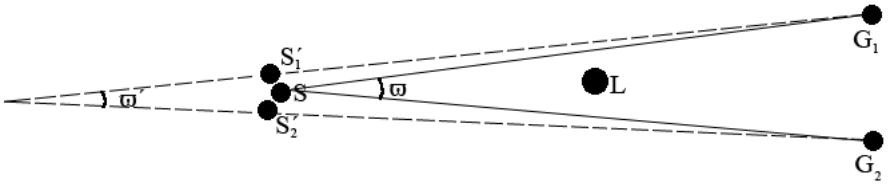

Figure 4.24: The panel above depicts how the effect observed in Fig. 4.9 arises. L is the lens and S is the true position of the source. S_1' is the position of the Source as seen by Gaia from G_1. Likewise for S_2' and G_2. ϖ is the true parallax (twice the parallax to be precise) and ϖ' is the resulting measured parallax. The schematic illustration clearly demonstrates that $\varpi > \varpi'$, i.e. that a lensed source will appear to be farther away.

This effect could be useful in confirming suspected lenses as it would be hard for any other thing to replicate the effect of shifting zero-parallax objects to negative values. It is however unlikely that Gaia will be able to utilize this effect since the zero parallax objects do not have a parallax of exactly 0.

These objects consist of galaxies, quasars and faint halo stars. The precision on the measurements determines the width of the distribution of parallaxes around zero of the objects. Figure 4.9 shows the change in parallax induced by a Jupiter at $\sim$ 50 AU and it is $\sim 40\mu as$. This is lower than the precision of the measurements for faint objects and what is shown in that case is an unrealistic situation. Besides that, there are not that many of these objects so having one close enough to a suspected lens is not probable.

Combining astrometric and photometric lensing

The relationship between astrometric and photometric lensing is quite interesting. There are few things that can cause such a characteristic increase and subsequent decrease in flux as a lensing event whereas the positional measurement of a source being off its expected value can caused by a variety of different reasons. On the other hand, detecting a photometric lensing event gives less information about the lens than an astrometric measurement.[4] Gaia however will be a lot more sensitive to astrometric shifts ($\sim 10^{-9}$) than it will be to photometric shifts ($\sim 10^{-3}$) and the two effects scale in a similar manner with angular separation between source and lens. This means that every photometric lensing event measured by Gaia also will measure the astrometric shift occurring at the same time. This is good because Gaia is designed to focus on sources that exhibit a rapid change in flux. That means that these lensing events will be fairly easy to detect and when they are, the patterns in the astrometric measurements can be studied. As stated, the astrometry is a lot more sensitive than the photometry which will result in a lot of astrometric lensing events being measured by Gaia during which there will be no detectable change in photometry. However, by studying the astrometric measurements done during photometric lensing events one could learn how to better identify purely astrometric lensing events using methods.

4.4 Summary

In this work three things have been explored; A somewhat direct method of detecting lenses in the Gaia data, if it is possible fit a lensing model to the lens detected in the observed data (i.e. determine its mass and position) and if it is possible to determine the mass of known bodies using their gravitational deflection of light. We have shown that with the selected criterion for what constitutes as a detection, having three adjacent sources with a large deviation from the expected errors (3σ), it is unlikely that any detections will be made. It must however be stressed that this criterion is for the detection of a lens and not a single lensing event. Having three sources with such large perturbations would mean that there would have to have been many measured lensing events for each source. This means that the number of predicted detections (~ 0.004) is not the same as the number of predicted lensing events (Belokurov & Evans, 2002). These events will be hard to find in the data as there will be some 10^{11} measurements to look through and one also has to be able to determine whether a given outlier is due to a lensing event and not something else. Besides that the predictions have been shown to be sensitive to many different factors, including assumed source density, line of sight density of lenses and the direction (and thus number of scans and size of the lens' parallax motion) one choses to look in. As an example, by relaxing the detection criterion to only needing one highly perturbed source we get the number of detections to be ~ 4.

If a lens is discovered in the data fitting the model attempted in this work will not be possible and that is primarily due to the problem being highly non-linear as can be seen in Eqs. 3.29, 3.30 and 3.31.

[4] A photometric lensing event can not tell more than the magnitude of the event, whereas an astrometric measurement gives both the magnitude and the direction to the lens relative source. Not only does one get extra information by knowing the direction to the lens, but being able to combine the two quantities allows for even more information to be deduced.

Solving the non-linear system of equations is not the problem in itself, the problem is the manner in which it has to be solved. In order to accurately fit the model, especially in the case where the signal is weak, a lot of sources have to be used as part of the fitting. Using a non-linear algorithm with as large a data set as one would like to use for this problem is computationally unfeasible.

Solving for the mass of visible bodies is probably one of the things which will be the most straight forward uses of lensing once the Gaia data comes in. However the mass will in all likelihood not be determined with the method tested in this work as the solutions tend to become unstable due to numerical effects. Either the algorithm used here could be redesigned in order to be able to better solve for distant bodies or methods such as the one discussed in section 4.3.2 can be used. As it stands, the only interesting realistic body for which the mass could be determined is the hypothesized massive planet in the inner outer Solar System, albeit solving for masses of bodies in the inner Solar system such as asteroids, planetesimals and dwarf planets warrant more investigation.

4.5 Future prospects

An immidiate followup to this work would be to investigate the possibility of direct mass determinations in optical binaries as it is the only thing that can be done that would not be heavily reliant on assumptions at the moment. As it stands, Gaia is in all likelihood precise enough to detect a lot of bodies by looking at the induced astrometric shift. The problem now however is that how this should be done in the best possible manner is not known yet. It is however nearly a decade until these kinds of studies will be doable with the real data so there is plenty of time to develop and test the tools. During this time the preliminary data releases of Gaia will be made available, the precision in these will not be sufficiently high to find anything but the strongest lenses. What this data will be useful for is making predictions and testing whatever statistical tools are being developed for the detection of lenses and lensing events. This work has shown that what can be seen in the observational residuals is heavily dependent on the assumptions made about the sources and the Galaxy. Thus, the first data releases will provide a sound basis for making these assumptions and will be useful when attempting to predict what can be seen in the final data release.

In the future if there ever is an astrometric mission which is meant as a lensing survey it does not have to be more precise than Gaia. The precision is sufficient, what would be needed is similar precision for the dim sources as Gaia currently has for the brightest sources and it should be designed in such a manner that most measurements are done in the direction of highest source density. This will allow for significantly more detected lensing events than Gaia and even stronger constraints on the population of invisible bodies.

If an astrometric mission aiming for nanoarcsecond accuracy is ever presented it will have to be able to account for these invisible bodies as they will perturb the observations significantly. Even the smaller bodies in the outer Solar system should be seen in the observational residuals of such a mission and the different patterns discussed in the Section 4.1 will likely appear. In addition to the even more detailed map of the visible part of the Galaxy than we will get from Gaia such a mission would also give a detailed map for the invisible part of the Galaxy.

Bibliography

Belokurov, V. A., & Evans, N. W. 2002, Monthly Notices of the Royal Astronomical Society, 331, 649

Byl, J. 1983, Moon and Planets, 29, 121

Davis, M., Hut, P., & Muller, R. A. 1984, Nature, 308, 715

de Bruijne, B. 2009, Gaia Technical Note ESA-JDB-053-01

Eddington, A. S. 1919, Nature, 104, 372

Farrell, S. A., Webb, N. A., Barret, D., Godet, O., & Rodrigues, J. M. 2009, Nature, 460, 73

Feissel, M., & Mignard, F. 1998, Astronomy and Astrophysics, 331, L33

Fender, R. P., Maccarone, T. J., & Heywood, I. 2013, Monthly Notices of the Royal Astronomical Society, 430, 1538

Gaudi, B. S., & Bloom, J. S. 2005, The Astrophysical Journal, 635, 711

Gould, A., & Salim, S. 1999, The Astrophysical Journal, 524, 794

Hobbs, D., Holl, B., Lindegren, L., et al. 2010, in IAU Symposium, Vol. 261, IAU Symposium, ed. S. A. Klioner, P. K. Seidelmann, & M. H. Soffel, 315–319

Holl, B. 2012, Gaia Technical Note LU-BH-003-01

Holl, B. Lindegren, L. H. D. 2009, Gaia Technical Note LU-BH-002-01

Kiziltan, B., Kottas, A., De Yoreo, M., & Thorsett, S. E. 2013, The Astrophysical Journal, 778, 66

Klioner, S. A. 2003, Astronomical Journal, 125, 1580

—. 2004, Physical Review D: Particles, Fields, Gravitation and Cosmology, 69, 124001

—. 2008, Gaia Technical Note LO-SK-006-2

Klioner, S. A., & Kopeikin, S. M. 1992, Astronomical Journal, 104, 897

Kroupa, P. 2001, Monthly Notices of the Royal Astronomical Society, 322, 231

Lindegren, L., Lammers, U., Hobbs, D., et al. 2012, Astronomy and Astrophysics, 538, A78

Lindegren, L., Hog, E., van Leeuwen, F., et al. 1992, Astronomy and Astrophysics, 258, 18

Luhman, K. L. 2014, The Astrophysical Journal Letters, 786, L18

Maccarone, T. J. 2005, Monthly Notices of the Royal Astronomical Society, 360, L30

Matese, J. J., Whitman, P. G., & Whitmire, D. P. 1999, Icarus, 141, 354

Matese, J. J., & Whitmire, D. P. 2011, Icarus, 211, 926

Melott, A. L., & Bambach, R. K. 2010, Monthly Notices of the Royal Astronomical Society, 407, L99

—. 2013, The Astrophysical Journal, 773, 6

Murray, C. A. 1983, Vectorial Astrometry (CRC Press)

Noyola, E., Gebhardt, K., Kissler-Patig, M., et al. 2010, The Astrophysical Journall, 719, L60

Özel, F., Psaltis, D., Narayan, R., & McClintock, J. E. 2010, The Astrophysical Journal, 725, 1918

Perryman, M. A. C., & ESA, eds. 1997, ESA Special Publication, Vol. 1200, The HIPPARCOS and TYCHO catalogues. Astrometric and photometric star catalogues derived from the ESA HIPPARCOS Space Astrometry Mission

Rashkov, V., & Madau, P. 2014, The Astrophysical Journal, 780, 187

Raup, D. M., & Sepkopski, J. J. 1984, Proceedings of the National Academy of Sciences, 811, 801

Sartore, N., Ripamonti, E., Treves, A., & Turolla, R. 2011, Advances in Space Research, 47, 1294

Smart, A. 2012, Gaia Technical Note OATO-RLS-005-1

Trujillo, C. A., & Sheppard, S. S. 2014, Nature, 507, 471

Zwicky, F. 1937, The Astrophysical Journal, 86, 217

Appendices

Appendix A

Gaia Relativistic Model (GREM)

In our tests we use a model based on the model developed for the Hipparcos mission Lindegren et al. (1992). Gaia itself uses a more rigorous model for light deflection, but for modeling the lens the Hipparcos model is sufficient. The model Gaia uses is the so called Gaia Relativistic Model (GREM) and is based on the model proposed by Klioner & Kopeikin (1992) and then later refined by Klioner (2003). First, a brief overview will be given of GREM and then a more detailed description of the model used in this project will be presented starting with showing its compatibility with GREM.

Figure A.1 shows everything that is going on. A source sends out light in the direction σ at negative infinity[1], as this light enters the Solar system its trajectory gets bent. Gaia, which is looking in the direction $\mathbf{s}$ observes the light coming from the source in the direction $\mathbf{n}$. Then, by knowing the ephemeris of the Solar system objects we can calculate the proper direction to the source, $\mathbf{k}$. After this it is only a matter of a simple transformation to the barycentric celestial reference frame (BCRS) and getting the direction, $\mathbf{l}$ to the source. It should be noted that all of these vectors are 3D unit vectors, i.e. $n \cdot n = n^1 n^1 + n^2 n^2 + n^3 n^3 = 1$ and their only purpose is to point in a specific direction. The steps Gaia takes are $\mathbf{s} \rightarrow \mathbf{n} \rightarrow \sigma \rightarrow \mathbf{k} (\rightarrow \mathbf{l})$

- $\mathbf{s} \rightarrow \mathbf{n}$
  The transformation is done by:
  $$\mathbf{s}' = -\mathbf{n} + \mathcal{O}(c^{-4}) \tag{A.1}$$
  $$\mathbf{s} = \left(\mathbf{s}' + \left\{ \frac{\Gamma}{c} + [\Gamma - 1] \frac{\mathbf{v} \cdot \mathbf{s}'}{|\mathbf{v}|^2} \right\} \mathbf{v} \right) \frac{1}{\Gamma (1 + \mathbf{v} \cdot \mathbf{s}'/c^2)} \tag{A.2}$$
  where
  $$\Gamma = \frac{1}{\sqrt{1 - |\mathbf{v}|^2/c^2}} \tag{A.3}$$
  and
  $$\mathbf{v} = \dot{\mathbf{x}}_\mathbf{0} \left(1 + \frac{1}{c^2} (1 + \gamma) w(\mathbf{x_0}) \right) + \mathcal{O}(c^{-4}) \tag{A.4}$$
  in which
  $$w(\mathbf{x}) = \sum_B \frac{G M_B}{r_{0B}} \tag{A.5}$$
  here, B is the index of the solar system objects and M_B is their corresponding mass. $r_{0B} = x_0(t_0) - x_B(t_0)$ where $|\mathbf{r_{0B}}| = r_{0B}$ and $\mathbf{x_B}(t)$ is the position of body i at time t taken from

[1] Since the position of the source is not known *a priori* the construction of having the vector point from an infinite distance is used.

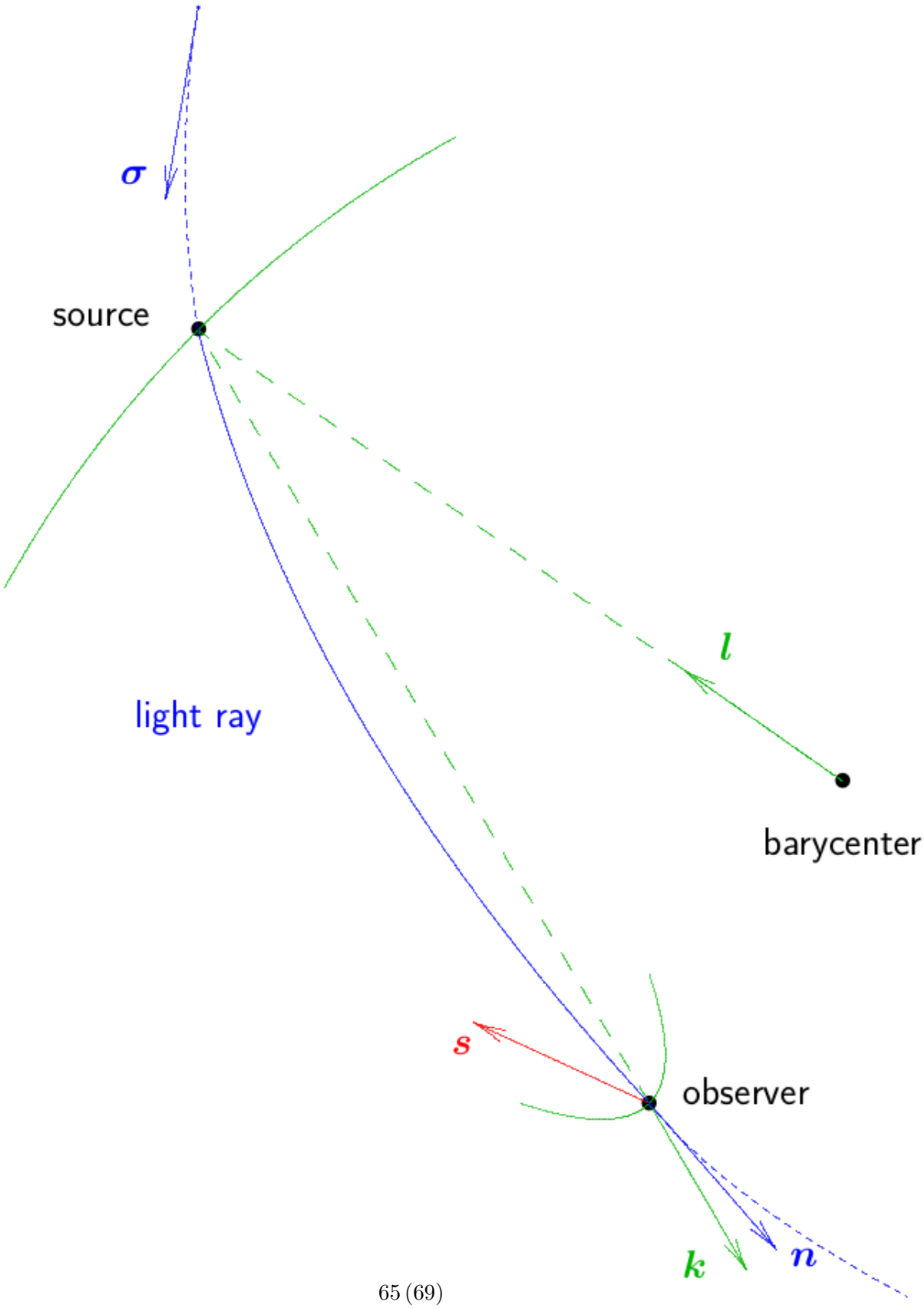
σ
source
l
light ray
barycenter
s
observer
k
n

the solar system ephemeris. γ is the parameter from the PPN-formalism which determines how space-time is curved by mass, in general relativity it is set to 1. Equation 4 shows the so called velocity normalization, for moderate observer velocities ($\sim$ 10km/s) the effect is on the level of a few μas. Thus, we generally only consider the solar potential in (5) when calculating (4) unless a greater accuracy than $\sim 10\mu$as is desired.

- $\mathbf{n} \rightarrow \mathbf{k}$
  The transformation is

$$\mathbf{n} = \sigma + \delta\sigma_{pN} + \delta\sigma_Q \tag{A.6}$$

Here the $\delta\sigma_{pN}$ is the gravitational deflection due to the monopole gravitational field of the solar system bodies, and $\delta\sigma_Q$ is the deflection due to their quadrupole gravitational field. Higher order terms are not of interest for Gaia unless the accuracy is to go down below 1 μas.
Assuming the source is farther than 1 pc away, one gets a simple relation between $\mathbf{k}$ and σ:

$$\mathbf{k} = \sigma + \text{terms less than } 0.1 \ \mu\text{as} \tag{A.7}$$

The total monopole deflection is given by:

$$\delta\sigma_{pN} = -\sum_B \frac{(1+\gamma)GM_B}{c^2} \frac{\mathbf{d}_B}{|\mathbf{d}_B|^2}(1 + \sigma \cdot \hat{\mathbf{r}}_{oi}) \tag{A.8}$$

Here, a hat denotes normalisation, i.e. $\hat{\mathbf{r}} = \mathbf{r}/|\mathbf{r}|$ and:

$$\mathbf{d}_B = \sigma \times (\mathbf{r}_{0B} \times \sigma) \tag{A.9}$$

where the '$\times$' of course is the vector product. What is important here is that the position each body i is calculated at a retarded* moment of TCB:

$$\mathbf{r}_{oi} = \mathbf{x}_0(t_0) - \mathbf{x}_B(t^*) \tag{A.10}$$

$$t^* = t_0 - \frac{1}{c}|\mathbf{x}_0(t_0) - \mathbf{x}_B(t^*)| \tag{A.11}$$

Eq. A.11 we can calculate as:

$$t^* = t_0 - \frac{|\mathbf{p}|^2}{c|\mathbf{p}| - \dot{\mathbf{x}}_B(t_o) \cdot \mathbf{p}}, \qquad \mathbf{p} = \mathbf{x}_o(t_o) - \mathbf{x}_B(t_0) \tag{A.12}$$

This makes the calculation a lot easier.

In the steps described above we have to evaluate the ephemeris of the deflecting bodies at three separate occasions (twice for position and once for velocity). This is a time consuming process and it would be optimal to reduce the number of evaluations. Klioner & Pip (ref) have shown that the same monopole deflection can be calculated using another set of equations, which only requires two evaluations of the ephemeris and gives a higher accuracy. This monopole deflection is given by:

$$\delta\sigma_{pN} = -\sum_B \frac{(1+\gamma)GM_B}{c^2} \left(\frac{\sigma \times (\rho_{oi} \times \mathbf{g}_B}{\delta_B^2}(1 + \hat{\mathbf{g}}_B \cdot \hat{\rho}_{0B}) - \frac{\sigma \times (\mathbf{k}_B \times \sigma}{|\rho_{0B}|} \right) \tag{A.13}$$

In which:

$$\mathbf{k}_B = \frac{1}{c}\dot{\mathbf{x}}(t_0) \tag{A.14}$$

$$\mathbf{g}_B = \sigma - \mathbf{k}_B \tag{A.15}$$

$$\rho_{0B} = \mathbf{x}_0(t_0) - \mathbf{x}_B(t_0) \tag{A.16}$$

Once again, a hat means normalization. And δ is the impact parameter, analogous to the one discussed in section ??? when talking about the thin lens approximation. Which means that it is the minimal distance between the light ray and the body, given by:

$$\delta_B = |\hat{\mathbf{g}}_B \times \rho_{0B}| \tag{A.17}$$

Appendix B

Linear least squares

Some of the problems that arise when trying to determine masses of lenses arise due to the way in which linear systems of equations are solved, because of that a short explanation is given in this Appendix. The method works as follows:
Given:

$$A \in \mathbb{R}^{m \times n} \tag{B.1}$$

we want to find a solution for

$$Ax \approx b \tag{B.2}$$

If $m = n$ and non-singular the problem is invertible and we can find an exact solution for $Ax = b$ which then simply is $x = A^{-1}b$. Otherwise, if $m > n$ the problem is said to be overdetermined or underdetermined if $m < n$. We attempt to find a solution by finding vectors in x that minimize the norm of squares of the residual $Ax - b$, which solves:

$$\min_{x \in \mathbb{R}^n} ||Ax - b||^2 \tag{B.3}$$

A way of directly solving this problem is to find the directional derivatives of x in the directions δx, it is given by:

$$\nabla ||Ax - b||^2 \delta x = 2\langle A\delta x, b - Ax\rangle = 2\delta x^T (A^T b - A^T x) \tag{B.4}$$

The minimum is found when all the directional derivatives are zero, this gives the normal equations

$$A^T Ax = A^T b \tag{B.5}$$

This rearranged gives:

$$x = (A^T A)^{-1} A^T b = A^\dagger b \tag{B.6}$$

Where $(A^T A)^{-1} A^T$ is known as the pseudoinverse of A.

Appendix C

Initial Mass Functions (IMFs)

The figure below shows a variety of different initial mass functions plotted on top of each other:

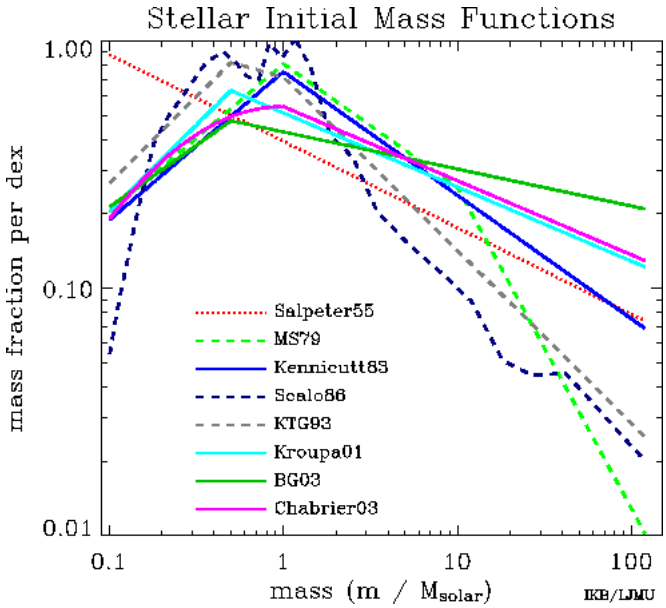

Figure C.1: The figure shows the different initial mass functions plotted together. The IMF tells us how stellar masses are distributed when stars form. All of the models are fairly similar in the mass range where we find the most common stars yet differ greatly for higher masses.
Image Credit: Ivan Baldry - http://www.astro.ljmu.ac.uk/ ikb/research/imf-use-in-cosmology.html